Prominent role of multi-scale microstructural heterogeneities on superplastic deformation of a high solid solution Al–7Mg alloy

Min Zha[1,6], Hongmin Zhang[1], Hailong Jia[1,6], Yipeng Gao[1,6], Shenbao Jin[3], Gang Sha[3], Ruben Bjørge[4], Ragnvald H. Mathiesen[5], Hans J. Roven[2], Huiyuan Wang[1,6*], Yanjun Li[2*]

1. Key Laboratory of Automobile Materials of Ministry of Education & School of Materials Science and Engineering, Nanling Campus, Jilin University, No. 5988 Renmin Street, Changchun 130025, PR China

2. Department of Materials Science and Engineering, Norwegian University of Science and Technology, 7491 Trondheim Norway

3. Herbert Gleiter Institute of Nanoscience & Department of Materials Science and Engineering, Nanjing University of Science and Technology, Nanjing 210094, China

4. SINTEF Materials and Chemistry, 7465 Trondheim, Norway

5. Department of Physics, Norwegian University of Science and Technology, 7491 Trondheim Norway

6. International Center of Future Science, Jilin University, Changchun 130012, PR China

Abstract

Achieving high superplasticity in single-phase Al alloys remains a challenge, since the fine-grained structure required for superplastic deformation coarsens rapidly in the absence of dispersed second-phase particles during tensile deformation at elevated temperatures. This paper concentrates on the superplastic response of a high solid solution Al–7Mg alloy processed by equal-channel angular pressing (ECAP) under uniaxial tension. The ECAP-processed Al–7Mg alloy features multi-scale microstructural heterogeneities including a bimodal grain structure and Mg solute segregation along grain boundaries (GBs) of nano/ultrafine grains. To identify effects of multi-scale microstructural heterogeneities on superplastic deformation behavior of the high solid solution Al–7Mg alloy, microstructural evolutions are studied systematically by combing electron backscatter diffraction (EBSD), ASTAR-transmission electron microscopy (TEM) orientation imaging and atom probe tomography (APT). During deformation at the optimal tensile condition of 573 K and 1×10^{-3} s^{-1}, the heterogeneous microstructure evolves to a stable uniform fine grain structure via continuous dynamic recrystallization (CDRX), and impressive superplasticity of ~523% elongation is achieved. The high superplasticity is discussed in terms of the cooperated mechanism by dislocation slip accommodated by CDRX at the early tensile deformation stage and grain boundary sliding (GBS) at the late

* Corresponding author. Tel/fax: +86 431 8509 4699
E–mail address: wanghuiyuan@jlu.edu.cn (Hui-Yuan Wang); yanjun.li@ntnu.no (Yan-Jun Li)

deformation stage. Our findings show that the evolution of microstructural heterogeneities in high solid solution Al–Mg alloys can be regulated, favoring for superplastic deformation, which offers an alternative strategy for developing low-cost Al alloys for enhanced mechanical properties.

Keywords: Inhomogeneous material; Microstructures; Grain boundaries; Thermomechanical processing; Superplasticity

1. Introduction

Al–Mg alloys are increasingly being applied in light-weight structural applications in aerospace and automotive industries to improve their fuel economy and reduce greenhouse gas emissions (Jobba et al., 2015; Kabirian et al., 2014; Koju and Mishin, 2020; Reyne et al., 2020). However, their usage is being limited mainly arising from their lower formability at room temperature and undesirable surface finish during sheet metal forming (Jobba et al., 2015; Kabirian et al., 2014). Due to their interactions with crystalline defects including dislocation and grain boundary (GB), solute Mg atoms play a critical role on the microstructural evolution and deformation behaviours of high solid solution Al–Mg alloys. Upon elevating temperatures, the Portevin-Le Chatelier (PLC) effect, i.e. flow instability, prevailing in Al–Mg alloys would disappear and ductility increases due to increased atom mobility and facilitated dislocation climb, accompanying with positive strain rate sensitivity, m (Pandey et al., 2013). In particular, superplasticity at high temperatures, i.e. huge plastic strains beyond hundreds of percent, has been extensively studied in high-specific strength Al–Mg based alloys from scientific and engineering perspectives, as the superplastic forming (SPF) technique enables near-net-shape manufacturing (Masuda and Sato, 2020).

It is well known that superplasticity is mainly caused by grain boundary sliding (GBS) mechanism. The enhanced ductility associated with GBS is attributed to the considerable increase in m values. The m index increases to 0.3–0.7 with GBS in a certain range of temperature, strain rate and grain size (Masuda and Sato, 2020). The increasing m index represents the enhanced ability to resist neck deformation at macroscopic scales, which leads to considerable ductility (Jia et al., 2019; Liu et al., 2020; Masuda and Sato, 2020). Thereby, superplastic alloys generally have been designed by the following principles: (i) achieving a uniform fine equiaxed grain structure (Avtokratova et al., 2012),

to increase GB density and enhance GB plasticity, and (ii) enhancing the thermal stability of fine grain structure at elevated temperatures by pinning GBs, employing multiphase structures and dispersed fine second-phase particles (Masuda and Sato, 2020).

Superplasticity in Al–Mg based alloys processed by severe plastic deformation (SPD) techniques, e.g. equal-channel angular pressing (ECAP), friction stir processing (FSP) and high-pressure torsion (HPT), has been studied widely in the last two decades (Avtokratova et al., 2012; Chuvil et al., 2021; Malopheyev et al., 2016). To obtain stable ultrafine-grained structures and high superplasticity with large elongations, Sc and/or Zr are often added into Al–Mg alloys prepared by SPD, as the coherent nano-sized Al_3Sc or $Al_3(Sc,Zr)$ precipitates generated upon SPD can effectively restrain grain growth during hot tensile deformation (Avtokratova et al., 2012; Chuvil et al., 2021; Duan et al., 2017; Malopheyev et al., 2016; Yang et al., 2016). However, the high cost of alloying elements, especially Sc, restricts their widespread commercial applications. In contrast, little attention has been paid to hot tensile deformation of single-phase Al–Mg alloys because of their relatively poor thermal stability (Meng et al., 2019). Especially, for SPD-processed Al–Mg alloys, the GBs of nano/ultrafine grains in general have high-energy non-equilibrium configuration, which are extremely unstable (Sauvage et al., 2012).

Non-equilibrium GBs in ultrafine-grained alloys processed by SPD are preferential sites for solute segregation and atomic clustering (Sauvage et al., 2014; Tugcu et al., 2012). Mg segregation along GBs and GB diffusion can impact the processing and mechanical properties of Al–Mg alloys (Koju and Mishin, 2020). As demonstrated by simulation studies and experimental results (Garner et al., 2021; Koju and Mishin, 2020; Zhang et al., 2019; Zhao et al., 2018; Sauvage et al., 2014; Liu et al., 2019), Mg atoms easily segregate along GBs and at triple junctions under severely deformed state. Using atom probe tomography (APT) technique, Mg-rich clusters (concentration in the range of 10–20 at.%) with sizes of 5–10 nm were revealed near GBs in a severely deformed Al–Mg alloy prepared by HPT (Sauvage et al., 2014). GB segregation was also detected in a HPT-processed Al–Mg alloy containing significantly less Mg in solid solution (0.5 wt.%) (Liu et al., 2019). In a recent study, concurrent Mg segregation along GBs and precipitation of nanoscale Al_3Mg_2 phase have been reported, which is responsible for enhancing grain coarsening resistance in nanocrystalline Al–Mg alloys during

annealing (Devaraj et al., 2019). It is thus expected that either the solute Mg segregation along GBs and/or the fine nanoscale Al_3Mg_2 precipitates could stabilize the ultrafine/nano grains and thus promote superplastic deformation of Al–Mg alloys during hot tensile deformation.

Tailored microstructural heterogeneities, including solute segregation along GBs (Bobylev et al., 2019; Liu et al., 2019) and heterogeneous structures, such as bimodal grain structure (Zhu and Lu, 2012), heterogeneous lamellar (Geng et al., 2020) and harmonic structure (Wang et al., 2020), have been demonstrated as effective strategies to improve mechanical properties of metallic materials. Thereinto, the heterogeneous microstructure offers the opportunity to reap benefits of the strong hardening capability from micron-sized coarse grains and high strength from nano/ultrafine grains, achieving satisfying strength-ductility synergy (Zhu and Lu, 2012). In particular, the high mechanical incompatibility between grains featuring different size scales during deformation would lead to hetero-deformation-induced hardening and contribute to extra strength (Ovid'ko et al., 2018). More recently, a new micromechanical model for heterogeneous nanograined metals has been developed, where the hetero-deformation in plastically deformable inclusions with different shapes is taken into consideration (J. Li et al., 2021). Nevertheless, according to conventional viewpoints, the bimodal grain structure seems not to benefit the activation of homogeneous GBS for superplastic deformation, since deformation mismatch easily exists in such heterogeneous microstructures (Bussiba et al., 2001).

In our previous studies, it was already demonstrated that by inducing bimodal grain structure together with fully utilizing the strong work-hardening effect of high-content solute Mg, both high strength and high ductility could be gained in the Al–7Mg alloy processed by ECAP, i.e., tensile strength of ~573–600 MPa and uniform ductility of ~14% (Zha et al., 2014, 2015a, 2015b). Recently, an Al–13Mg alloy processed by cold rolling was reported to feature an impressive yield stress of ~653 MPa and a maximum tensile strength of ~733 MPa but a much lower tensile elongation of ~5% (Jang et al., 2019). The high strength in Al–Mg alloys containing high solute Mg levels has been attributed to the intensified interactions of Mg atoms and dislocations, facilitating stronger accumulation of dislocations and a heterogeneous/bimodal microstructure containing nano-sized substructures and ultrafine grains (Zha et al., 2014, 2015a, 2015b, Jang et al., 2019). Whereas, the high uniform elongation in Al–7Mg is due primarily to the enhanced work hardening resulting from the high solute

Mg content and the bimodal grain structure; meanwhile, the dynamic strain aging (DSA) effect originating from the solute-dislocation interaction could also contribute to the high ductility (Zha et al., 2014, 2015a, 2015b).

Nevertheless, our previous studies have mainly focused on the role of bimodal grain structure on improved strength and ductility at room temperature of binary Al–Mg alloys processed by ECAP (Zha et al., 2014, 2015a, 2015b). Their mechanical behaviours at elevated temperatures remain unknown. Furthermore, the Mg GB segregation can affect deformation behaviours at both room and elevated temperatures. To the best of the authors' knowledge, however, it is still yet unknown to what extent the deformation conditions (e.g. the deformation temperature and strain rate) and inhomogeneous microstructural characteristics (e.g. the bimodal grain structure and Mg GB segregation) influence the mechanisms of superplastic deformation. It is thus of great interest to explore the mechanisms that govern superplasticity of high solid solution Al–Mg alloys featuring inhomogeneous microstructure at elevated temperatures.

For this purpose, the high solid solution Al–7Mg alloy processed by ECAP was selected and systematically investigated as to microstructural evolution and mechanical behaviours with different deformation parameters at elevated temperatures. In the present study, we found that the Al–7Mg alloy processed by ECAP to 4 passes exhibited a multi-scale microstructural heterogeneities and impressive superplasticity of ~523% elongation at the optimal tensile condition of 573 K and 1×10^{-3} s^{-1}, which is not accessible to previously reported uniform-grained dilute binary Al–Mg alloys. Thereby, systematic studies were carried out to explore microstructural evolution and superplastic deformation behaviors of such a material featuring multi-scale microstructural heterogeneities, by utilizing advanced electron microscopy techniques and APT techniques in conjunction with detailed analysis of grain growth kinetics.

The present article addresses the evolution of multi-scale heterogeneous microstructure during hot tensile deformation and focuses on understanding the roles of the bimodal grain structure and Mg segregation along GBs on superplastic response of the high solid solution Al–7Mg alloy under uniaxial tension. The work provides data that should help in better understanding of the influence of various microstructural heterogeneities on mechanical properties at elevated temperatures of binary high solid

solution Al–Mg alloys, which thus may offer an alternative strategy to design low-cost superplastic metallic materials.

2. Experimental procedure

Materials used in the present work were taken from Al–7Mg cast ingots supplied by Hydro Aluminum having chemical compositions (in wt.%): Mg 7.0, Fe 0.05, Si 0.06, with Al in balance. Before ECAP, the Al–7Mg ingots were cut into bars with 100.0 mm × 19.5 mm × 19.5 mm in size and then the bars were homogenized at 773 K for 3 h, followed by water quenching to room temperature. ECAP was performed with route B_c in a 90-degree die, which leads to an imposed strain of ~1.0 per pass. ECAP experiments were carried out at room temperature and the bulk Al–7Mg alloy was pressed successfully to a total of 2 and 4 passes. To achieve 4 passes, short-time inter-pass annealing (573 ± 3 K for 120 s) followed by water-quenching between the 2nd and 3rd passes was performed in a molten salt bath, to release residual stress after 2-pass ECAP. For convenience, ECAP bars going through x passes were labelled as xP (here x = 2 and 4) samples.

The specimens for EBSD studies were prepared by standard metallographic techniques followed by electro polishing using a solution of 80% C_2H_5OH + 20% $HClO_4$ at 20 V for 15–25 s at 243 K. EBSD detection was carried out in a Zeiss 55VP FEG-scanning electron microscopy (SEM) equipped with a Nordif EBSD detector and TSL OIM software, and performed at 20 kV, 20 mm working distance, 70^o tilt, and 0.05–0.5 μm scan steps. Low-temperature annealing at 200 ^{o}C for 30 min was conducted on ECAPed samples, to release partial strains and enhance the quality of Kikuchi patterns during EBSD detection. The microstructure information of low-temperature annealed samples can roughly represent that of the as-deformed samples (Zha et al., 2014). More details about EBSD metallographic sample preparation and the grain construction procedure during EBSD analysis are available in (Zha et al., 2014). Transmission electron microscopy (TEM) foils were prepared by twin-jet electro polishing in a solution of 33% nitric acid inmethanol at 243 K. The bright-field TEM analysis was performed with a Philips CM30 operating at 150 kV and a JEOL 2010 at 200 kV. The TEM orientation mapping was performed employing a JEOL ARM200CF at 200 kV equipped with the NanoMEGAS ASTAR system.

Tip samples for APT were prepared in a two-step electro polishing procedure with a thin bar having a cross-section of 0.5 mm × 0.5 mm. In the first step, the electrolyte of 25% perchloric acid in acetic acid at a direct current of 15 V was used. In the second step, the electrolyte was 4% perchloric acid in 2-butoxethynal and the operating parameters were 20 V at room temperature. APT characterization was performed in a local electrode atom probe (LEAP 4000X Si) with a specimen temperature of 26 K under UV laser pulsing with a wave length of 358 nm, a laser energy of 40 pJ and a target evaporation rate of 1%.

Specimens for tensile tests were machined from as-ECAPed samples along extrusion direction (ED), having a gauge size of 10.0 mm × 3.70 mm × 1.60 mm. Corresponding tensile tests were performed in an INSTRON 5869 testing machine at 423–623 K under strain rates of 5×10^{-4}–1×10^{-2} s^{-1}. Prior to hot tensile deformation, samples were held for 10 min at the test temperature to realize thermal equilibrium. For more reliable results, at least three samples were tested for each condition.

3. Results

3.1. Characterization of the heterogeneous microstructure

EBSD observations reveal that the 2P sample consists mainly of coarse elongated grains containing profuse low-angle grain boundaries (LAGBs) (Fig. 1(a)). In contrast, the 4P sample features a typical bimodal grain structure, composing of necklace-like recrystallized ultrafine grains and coarse-deformed grains of several micrometers in size (Fig. 1(c) and (e)). Such a bimodal microstructure containing nano-sized substructures and ultrafine grains has been reported in our previous work (Zha et al., 2014, 2015a, 2015b). Similar heterogeneous microstructures featuring different size scales were also reported in an Al–6.5Mg alloy prepared by high strain rate rolling (X. Li et al., 2021) and an Al–13Mg alloy with an exceptional high Mg content developed via cold rolling (Jang et al., 2019). According to the kernel average misorientation (KAM) maps, there are larger local strains in coarse-grained interiors of the 4P sample in comparison to the 2P sample (Fig. 1(b) and (d)), indicating a higher dislocation density preserved in the former. Moreover, in contrast to the lower fraction of high-angle grain boundaries (HAGBs) in the 2P sample, a large number of HAGBs,

accounting for ~60% of the total GBs, have generated in the 4P sample, further confirmimg the formation of considerable amounts of nano-sized/ultrafine (sub) grains (Fig. 1(f)). Nevertheless, few nano-sized substructures and/or ultrafine grains were observed in those high solid solution Al–Mg alloys processed by rolling processes where the relatively low accumulated strain was insufficient to induce extensive continuous dynamic recrystallization (CDRX) (X. Li et al., 2021, Jang et al., 2019).

Detailed orientation mapping using Nanomegas-ASTAR shows that mostly elongated nano/ultrafine grains form in the fine-grained region of the 4P sample (Fig. 2(a)), where the sizes of ~70% grains are smaller than 100 nm (Fig. 2(c)). Note that the fraction of HAGBs, i.e., f_{HAGBs} = 57%, measured from the ASTAR-TEM orientation map (Fig. 2(d)) agrees well with that obtained from the EBSD map, i.e., f_{HAGBs} = 60% (Fig. 1(f)), reflecting that the data obtained by both EBSD and Nanomegas-ASTAR analyses are sufficiently reliable. Moreover, the corresponding KAM map and local strain distribution chart (Fig. 2(b) and (e)) show high strains in nano/ultrafine grains, indicating there is still a high dislocation density preserved in the nano/ultrafine grains.

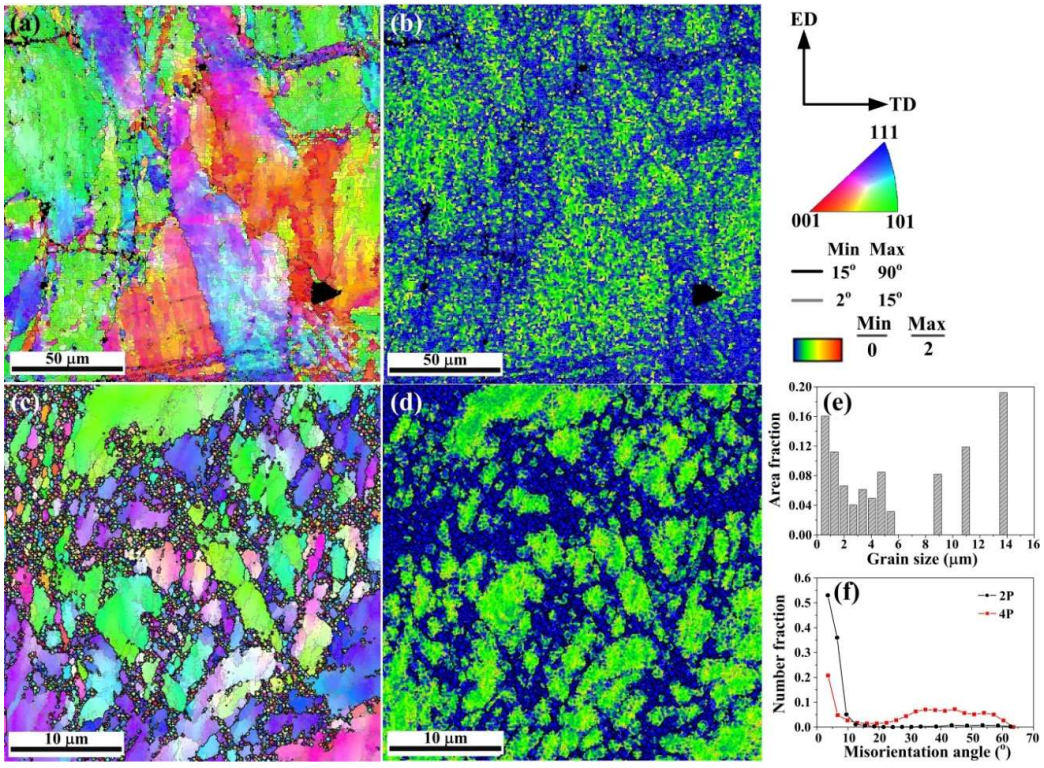

Fig. 1. (a) and (c) Inverse pole figure (IPF) maps as well as (b) and (d) KAM maps obtained by EBSD of ECAPed Al–7Mg samples: (a) and (b) the 2P sample, (c) and (d) the 4P sample; (e) the grain size distribution in area fraction of the 4P sample and (f) the GB misorientation angle distribution of 2P and 4P samples. The inset in top right is the color coded map for IPF maps.

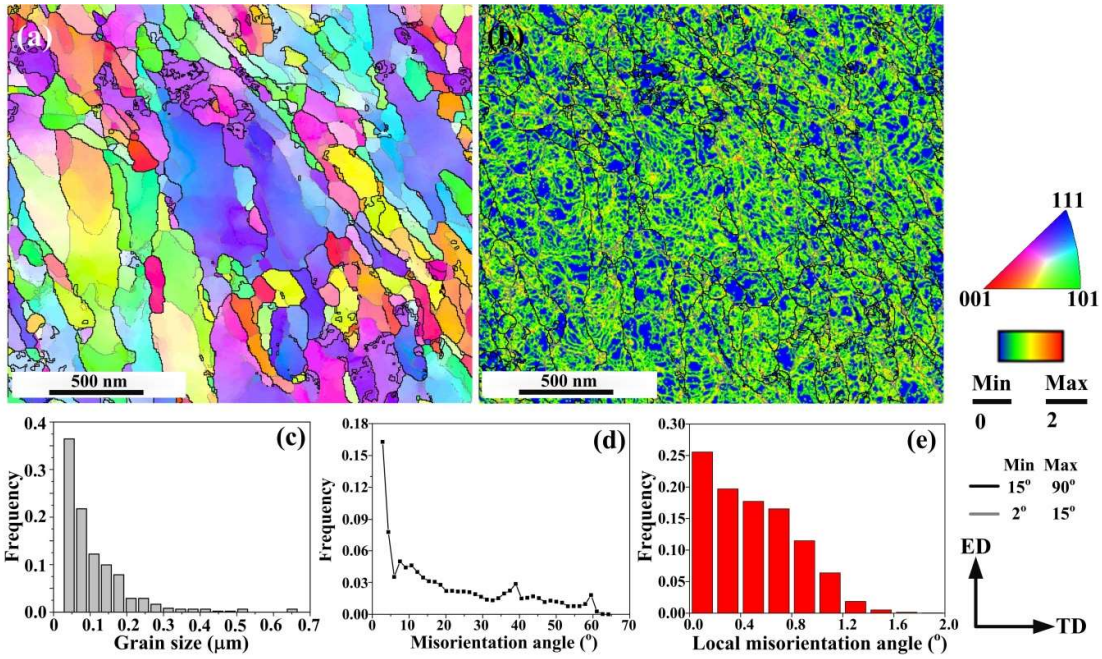

Fig. 2. (a) The representative ASTAR-TEM orientation image and (b) the KAM map of the 4P ECAPed Al–7Mg sample; (c–e) the corresponding distribution of grain size, GB misorientation angle and local misorientation angle, respectively. The inset in top right is the color coded map for orientation map.

Representative TEM images confirm that many equiaxed nano-sized grains < 100 nm together with elongated ultrafine grains (50–200 nm in width and 100–500 nm in length) have formed in the 4P sample (Fig. 3(b) and (c)). In contrast, mainly dislocation tangles and a few ultrafine equiaxed grains (~500 nm) have developed in the 2P sample (Fig. 3(a)). Furthermore, TEM studies reveal the existence of fuzzy GBs and a high dislocation density in grain interiors of the 4P sample (Fig. 3(d)), indicating non-equilibrium GB characteristics and large internal lattice stresses, which agrees well with aforementioned KAM analysis. In addition, TEM observations and selected area diffraction (SAD) show that Mg-containing precipitates have probably not formed in both samples (Fig. 3). It is consistent with our previous investigations on the Al–7Mg processed by ECAP, where many equiaxed nano-sized and elongated ultrafine grains were observed but no Mg-containing phases were detected (Zha et al., 2015a, 2015b).

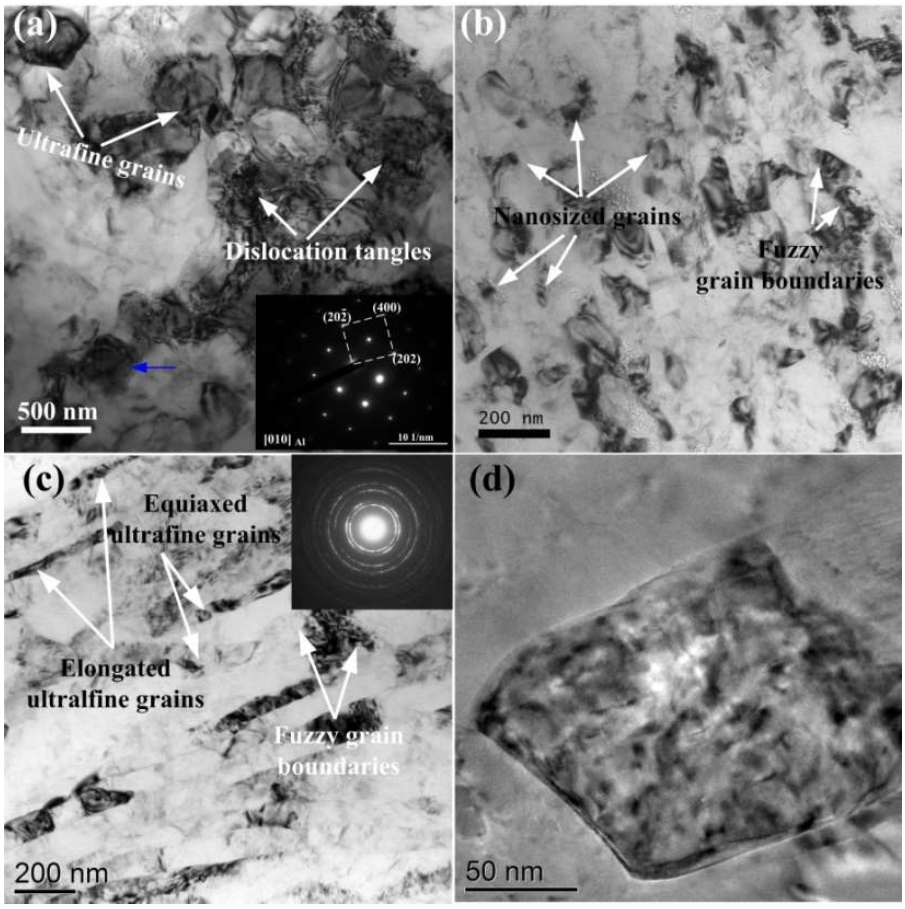

Fig. 3. Representative TEM images of ECAPed Al–7Mg samples: (a) the 2P sample and (b–d) the 4P sample. The inset in (a) is the diffraction pattern of the grain indicated by the blue arrow; the inset in (c) is the diffraction pattern of ultrafine grains.

3.2. The heterogeneous distribution of solute Mg and its GB segregation

Our previous investigations indicated that GB segregation of Mg solute might exist in the Al–7Mg alloy processed by room-temperature ECAP after 3 and 6 passes (Zha et al., 2015a). To reveal the likely Mg segregation at GBs, both scanning transmission electron microscopy (STEM) and APT analyses were conducted on the present 4P sample. During STEM detection, line scans with a step size of 0.4 nm were done along the selected GBs. The Mg concentration line profile across the GB in Fig. 4(a) clearly shows that solute Mg distribution is heterogeneous (Fig. 4(b)). Local fluctuations of Mg concentration exist, including a higher concentration peak at the GB, i.e. the Mg GB segregation (arrow 1) and a slightly lower concentration peak at some distance away from the GB (e.g. arrow 2).

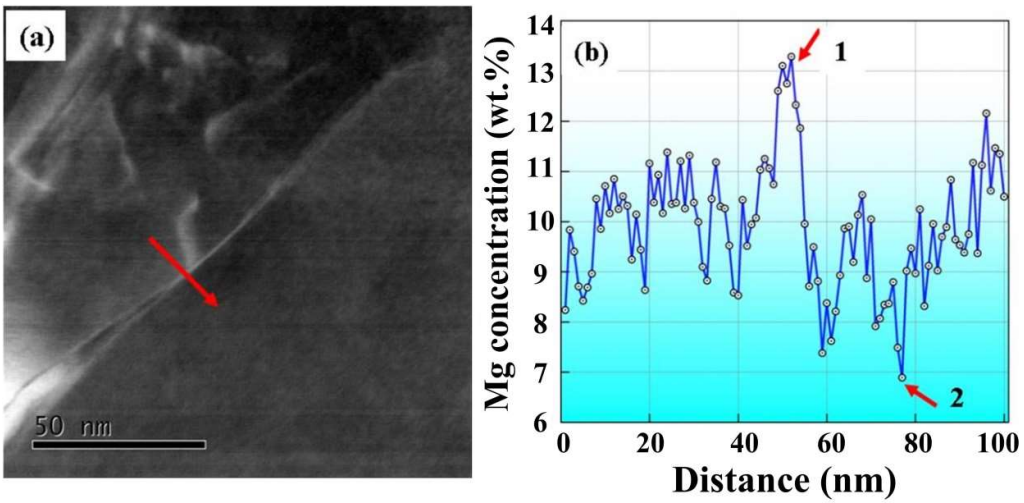

Fig. 4. (a) The high-angle annular dark field (HAADF) STEM image of the 4P ECAPed Al–7Mg sample and (b) the line profile of Mg concentration across the GB in (a), indicating the Mg segregation along the GB.

APT analyses were performed on several needle tip samples. The analyzed volume displayed in Fig. 5(a) and (b) contains a GB section and two regions highly enriching Mg atoms. A concentration profile taken across the GB reveals a higher Mg concentration (up to ~13 at.%) than the surrounding matrix, which is also higher than the nominal alloy composition (Fig. 5(c)). Such visible Mg GB segregation events have been frequently observed in previous work on Al–Mg alloys fabricated by SPD processing, like HPT and ECAP (Sauvage et al., 2012, 2014). The strong solute Mg segregation along GBs in the Al–Mg alloy could be partially attributed to the reduced GB energy via Mg segregation (D. Zhao et al., 2018). According to an atomistic study of GB segregation and GB diffusion in Al–Mg alloys, Mg atoms tend to segregate to a tilt GB and form clusters with highly anisotropic shapes at low temperatures (Koju and Mishin, 2020). Moreover, GBs are immobile sinks for vacancies (Li et al., 2015). Especially, some GBs in the SPD state are in non-equilibrium state having a disordered structure, acting as preferential segregation sites for Mg atoms (Sauvage et al., 2012). Therefore, due to the positive binding energy of Mg-vacancy clusters (Peng et al., 2020), vacancies tend to drag Mg atoms and diffuse towards (non-equilibrium) GBs and triple junctions of nano/ultrafine grains.

In addition, the local Mg concentration in a strong segregation region along the GB (lower left part in Fig. 5(b)) is in the range of ~30–40 at. % within a layer of ~4 nm in thickness (Fig. 5(d)). The region is most likely an Al_3Mg_2 precipitate since the detected Mg content is very close to that of the

intermetallic Al_3Mg_2 phase. The reason for not observing Mg-rich precipitates in previous careful TEM studies may be due to their small sizes, e.g. too small for significant diffraction signals. Also, the fraction of such precipitates may be too low to be detected by X-ray diffraction (XRD).

Actually, both the contribution of dislocations and deformation-induced vacancies were considered to account for the enhanced mobility of Mg atoms (Sauvage et al., 2012, 2014). The mechanisms controlling dynamic precipitation and segregation during SPD of Al alloys containing high levels of Mg have been discussed in detail in literature (Sauvage et al., 2014).

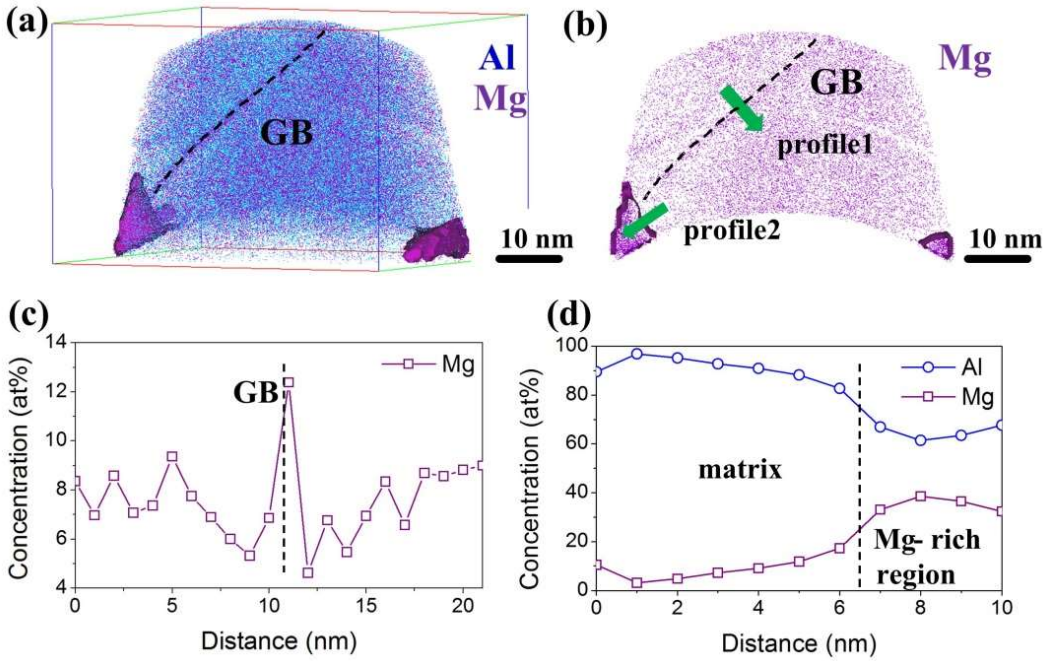

Fig. 5. APT analyses of the 4P ECAPed Al–7Mg sample: (a) and (b) element distribution maps, where Al (blue) and Mg (pink) atoms are clearly shown; (c) and (d) the concentration profile of Mg solute across the GB and local strong Mg-rich region along the GB, respectively, indicated by green arrows in (b), confirming the heterogeneous distribution of Mg atoms along the GB.

3.3. Tensile properties at elevated temperatures

Typical tensile stress-strain curves of the 2P and 4P Al–7Mg samples at varying strain rates and different temperatures are shown in Fig. 6. In the temperature range of 473–573 K and 5×10^{-4} s^{-1}, the coarse-grained 2P sample always presents lower elongations to failure than the bimodal-grained 4P one (Fig. 6(a)). When tested at 573 K, the elongation of the 4P sample increases from ~318% to ~523% with the strain rate increasing from 5×10^{-4} to 1×10^{-3} s^{-1}, but it decreases to ~325% with further increasing the strain rate to 1×10^{-2} s^{-1} (Fig. 6(b)). Meanwhile, flow stress increases monotonously

with increasing strain rates. In addition, the 4P sample exhibits relatively low elongations when tested at lower temperatures of 473–548 K, i.e. ~125–251%, or at elevated temperature of 623 K, i.e. ~155%, under the constant strain rate of 5×10^{-4} s^{-1}. Note that the bimodal-grained 4P sample possesses a much higher elongation than the 2P sample, i.e. ~523% *vs*. ~198%, at the optimal tensile condition of 573 K and 1×10^{-3} s^{-1} (Fig. 6(b)).

It is apparent that the elongation to failure of present binary Al–7Mg alloy is somewhat lower than the extensively studied Al–Mg alloys containing Sc and/or Zr prepared by similar ECAP processing (Avtokratova et al., 2012; Chuvil et al., 2021; Duan et al., 2017). A representative Al–3Mg–0.2Sc alloy subjected to 4-pass ECAP exhibited an elongation to failure of > 680% (Komura et al., 2001). It is due primarily to the coherent nano-sized precipitates formed in those Al–Mg alloys containing transient elements can pin GBs effectively, contributing to stabilize the fine grain structure. However, Sc and/or Zr are very costly and it is difficult to expand commercial applications of Al–Mg alloys containing Sc and/or Zr. In contrast, the present low-cost binary Al–7Mg alloy is more economical. Also, the > 500% elongation to failure at relatively high strain rate is adequate for superplastic manufacturing in industrial applications.

To investigate the dominant deformation mechanisms of present bimodal-grained 4P sample, experimental data on strain rate sensitivity (m) as a function of true strain were collected, see Fig. 6(c). Here, m is defined as $\partial \log\sigma / \partial \log\dot{\varepsilon}$, where σ is the true flow stress and $\dot{\varepsilon}$ is the strain rate (Kim et al., 2017). Upon tensile deformation at 548 and 623 K, m shows weak strain dependence with an average value of ~0.38 and ~0.26, respectively (Fig. 6(c)). This is consistent with the lower elongations to failure, i.e. ~250% and ~155%. In contrast, when tested at 573 K, the m value increases from 0.40 to 0.48 and further to 0.75 with the true strain increasing from 0.1 to 0.4 and further to 1.4 (corresponding to an elongation of ~10%, ~50% and ~300%, respectively). It suggests that GBS has been activated beyond ~50% elongation since the onset of GBS corresponds to an m value of ~0.5 (Liu et al., 2020). Also, the high positive m values agree well with the strong necking resistance and the high superplasticity. It distinguishes from the negative m values in Al–Mg alloys subjected to tensile deformation at room temperature, where DSA induced by the solute-dislocation interaction prevails, making itself felt as serrations on the stress-strain curve (Fu et al., 2012; Jobba et al., 2015).

The related studies on the DSA effect and its role on room-temperature ductility of the ECAPed Al–7Mg alloy have been clarified in our previous work (Zha et al., 2015a).

Furthermore, deformation activation energy (Q) is determined to reveal the controlling mechanism of the bimodal-grained 4P sample at the optimal strain rate of 1×10^{-3} s^{-1}, based on the Arrhenius equation (Mikhaylovskaya et al., 2014):

$$\dot{\varepsilon} = A\sigma^{1/m}e^{-Q/RT} \quad (1)$$

where $\dot{\varepsilon}$ is the strain rate, A is the constant of material, σ is the flow stress, R = 8.314 J/mol is the gas constant and T is the temperature. Note that σ is taken at the true strain of 0.4, i.e. ~50% elongation. The calculated Q value of ~78 kJ/mol (Fig. 6(d)) is close to that of the GB self-diffusion of Al alloys, i.e. 86 kJ/mol (Kawasaki et al., 2011). It further confirms that GBS controlled by GB diffusion has become the dominant superplastic deformation mechanism in the late deformation stage.

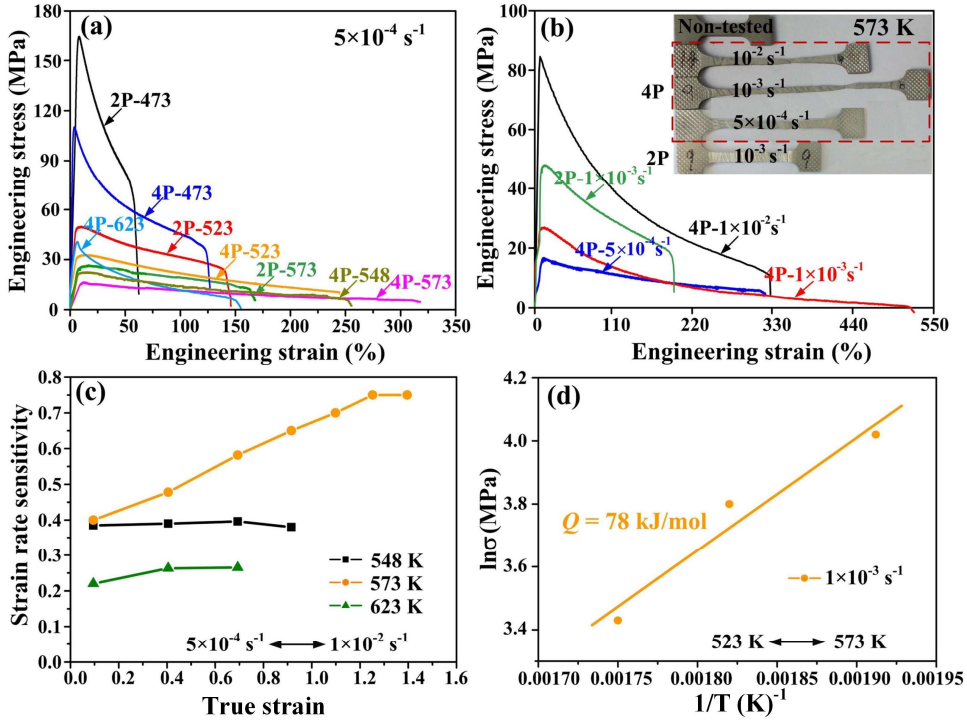

Fig. 6. Tensile engineering stress-strain curves of the 2P and 4P Al–7Mg samples tested at: (a) various temperatures and (b) various strain rates; (c) the variation of strain rate sensitivity with true strain of the 4P sample at different temperatures and (d) the variation of ln σ with 1/T derived from tensile stress-strain curves of the 4P sample at 1×10^{-3} s^{-1}. The inset in (b) shows pictures of tested tensile samples.

3.4. Microstructural evolution during hot tensile deformation

The superplastic deformation behaviors of the 4P Al–7Mg sample are closely related to the multi-scale microstructural heterogeneities and their evolutions upon hot deformation at various strain rates and test temperatures. Thereby, we conducted EBSD analyses on the gauge section of 4P samples subjected to tension and fractured at different temperatures and strain rates. As shown in Fig. 7(a), after tensile deformation at 548 K and 5×10^{-4} s^{-1}, equiaxed grains (~3 μm) form, accompanied with the reduced volume fraction of coarse grains (several microns). Note that this microstructural evolution is distinct from our previous work where mainly recovery occurred in the 3-pass ECAPed Al–7Mg alloy when annealed even for 96 h at 548 K (Zha et al., 2014). It can be rationalized by the extra strain induced during hot tensile deformation that accelerates the microstructural evolution process. In the sample tension fractured at 573 K with the same strain rate (Fig. 7(b)), complete recrystallization has occurred and a uniform fine grain structure with an average grain size of ~5 μm has formed. With increasing strain rate from 5×10^{-4} to 1×10^{-2} s^{-1}, finer equiaxed recrystallized grains of ~3 μm form (Fig. 7(c)). However, increasing the temperature further to 623 K leads to remarkable grain growth to ~20 μm (Fig. 7(d)).

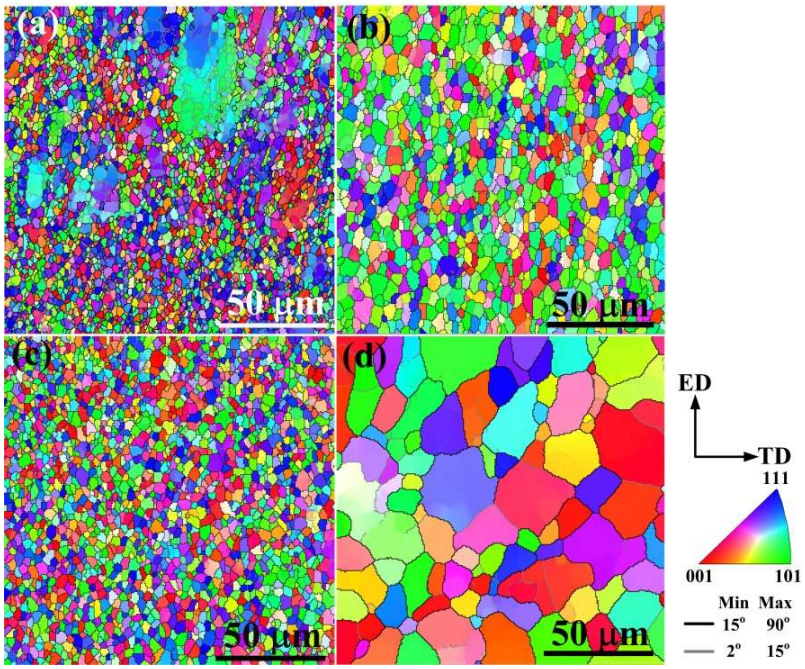

Fig. 7. Typical IPF maps obtained by EBSD of the 4P ECAPed Al–7Mg sample subjected to tension and fractured at: (a) 548 K and 5×10^{-4} s^{-1}, (b) 573 K and 5×10^{-4} s^{-1}, (c) 573 K and 1×10^{-2} s^{-1} as well as (d) 623 K and 5×10^{-4} s^{-1}. The inset in bottom right is the color coded map for IPF maps.

Microstructural evolution of the 4P sample during deformation at 573 K and 1×10^{-3} s^{-1} was traced by observing the gauge section of samples tensioned to ~10% (corresponding to the peak flow stress), ~50%, ~300% and upon fracture (~523%). The representative EBSD results are shown in Fig. 8. For comparison, information on the gauge section of 2P sample and the grip section of 4P sample tension fractured at 573 K and 1×10^{-3} s^{-1} is also provided (Figs. S1 and S2). At the elongation of ~10%, partial recrystallization occurs in initial coarse grains, accompanying with the formation of numerous (sub) GBs in grain interiors (Fig. 8(a)). The corresponding KAM map reveals that coarse grains possess much higher internal strains than fine grains (Fig. 8(e)). It indicates that there is a higher driving force for recrystallization to occur in coarse grains. The degree of internal strain gradually decreases and a large number of fine grains form with further deformation to ~50% (Fig. 8(b) and (f)). Almost all coarse grains have transformed into fine recrystallized grains at ~300% elongation (Fig. 8(c)), and a uniform fine grain structure (~3.6 μm) is well kept in the fractured sample (elongation ~523%) (Fig. 8(d)), which is clearly confirmed by the grain size distribution in Fig. 9(a). Meanwhile, the fraction of HAGBs increases prominently with deformation proceeding to ≥ 50% elongation at 573 K (Fig. 9(b)). In contrast, much coarser recrystallized (sub) grains have formed in the 2P sample after subjected to tension and fractured at 573 K and 1×10^{-3} s^{-1}, and lots of LAGBs still exist (Fig. S1).

The {110} and {111} pole figures show that the 4P Al–7Mg sample deformed to ~10% exhibits typical features of shear texture (Fig. 8(i)), which is still kept but the maximum intensity decreases significantly after ~50% tensile elongation (Fig. 8(j)). With further deformation to ~300% and till fracture, the texture distribution becomes gradually random with a very low intensity (Fig. 8(k) and (l)). In comparison, strong shear texture still maintains in the grip section of the same sample despite nearly complete recrystallization (Fig. S2).

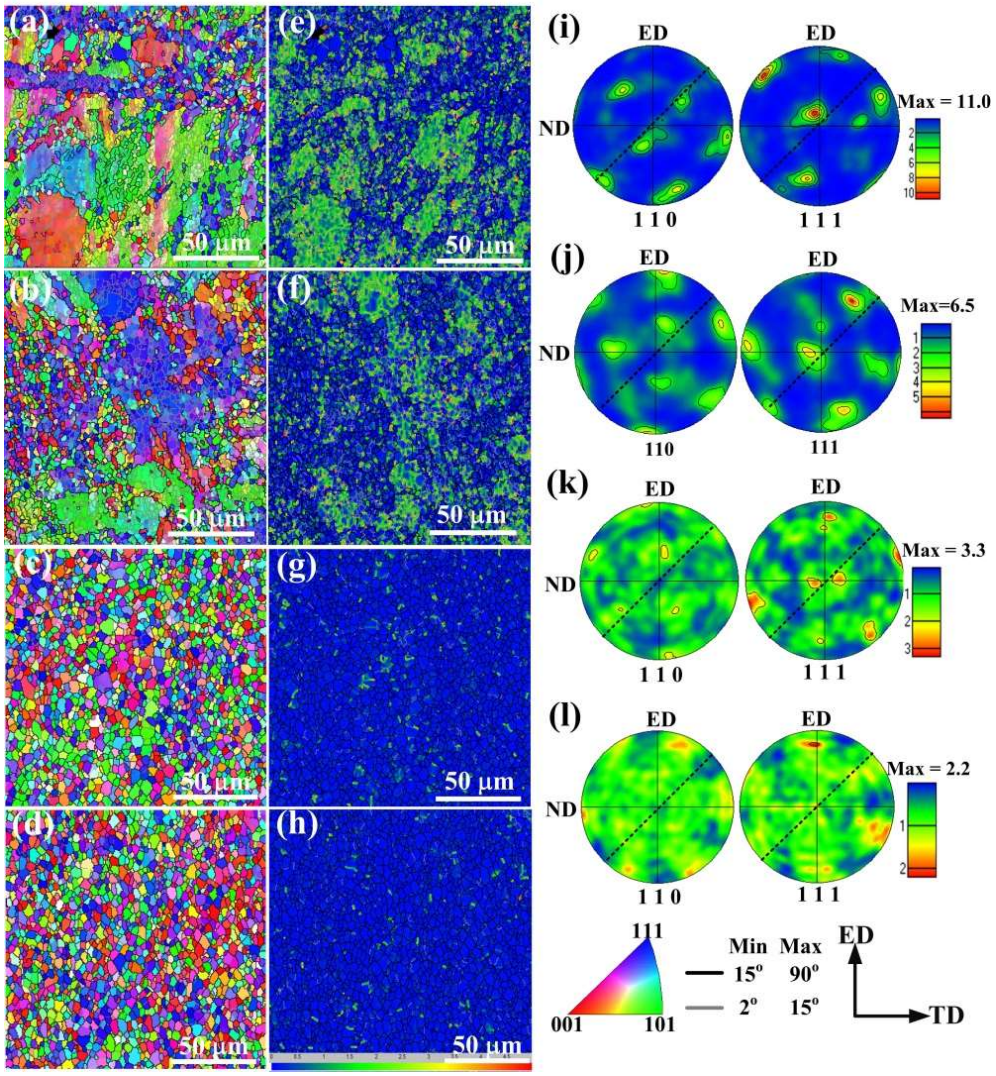

Fig. 8. (a–d) Typical IPF maps, (e–h) KAM maps as well as (i–l) {110} and {111} pole figures (in the ED-ND projection) obtained by EBSD for the 4P ECAPed Al–7Mg sample deformed at 573 K and 1×10^{-3} s^{-1} to a selected elongation: (a), (e) and (i) ~10%; (b), (f) and (j) ~50%; (c), (g) and (k) ~300%; (d), (h) and (l) ~523%. Dashed lines in pole figures represent the ideal shear plane. The inset in bottom right is the color coded map for IPF maps.

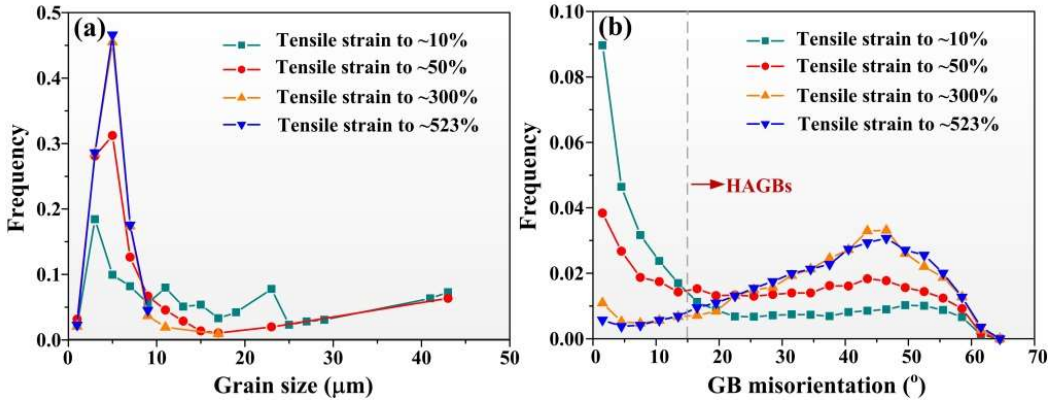

Fig. 9. The evolution of (a) grain size distribution and (b) GB misorientation angle distribution of the 4P ECAPed Al–7Mg sample during tensile deformation at 573 K and 1×10^{-3} s^{-1}.

One may expect Mg-containing precipitates to form in the high solid solution Al–7Mg alloy when deformed at 573 K for sufficiently long time, i.e. ~1.5 h, as both the supersaturation of solute Mg atoms in the matrix and Mg segregation along GBs favor precipitation. Therefore, TEM observations were conducted on the tension-fractured sample. The sample was machined from the region between gauge and grip section due to the difficulty in getting sufficient materials from the gauge section alone (see inset in Fig. 6(b)). Considering that the 4P sample was held in a furnace at 573 K for 10 min before tensile deformation, information on the statically annealed sample was also included for comparison.

TEM images show that ultrafine grains still exist after annealing at 573 K for 10 min (Fig. 10(a)), indicating these ultrafine grains possess a strong coarsening resistance. Meanwhile, dense dislocation tangles, i.e. high-density dislocations, are preserved (Fig. 10(b)), suggesting a high thermal stability against dislocation recovery. Note that no Mg-rich precipitates are detected in grain interiors or along GBs in this condition, as shown by a representative SAD pattern inserted in Fig. 10(b). It further confirms that solute Mg atoms are mainly in solid solution and GB segregation before tensile deformation, as revealed by Figs. 4 and 5. The notable coarsening resistance of ultrafine grains and preserved dislocation tangles can be attributed mainly to the strong Mg solute segregation along GBs and high-level solute Mg atoms in grain interiors, respectively.

In the fractured sample after superplastic deformation at 573 K, a large fraction of fine equiaxed recrystallized grains of 1–5 μm with equilibrium GBs (as indicated by the thickness fringes) exist, and most of the fine grains are nearly free of dislocations (Fig. 10(c) and (d)). The SAD analysis reveals that some nano-sized (several tens of nano meters) Al_3Mg_2 precipitates distribute in grain interiors and along GBs (see labels p_1–p_3 in Fig. 10(d)). The nano-sized Al_3Mg_2 precipitates observed inside grains (such as p_3 in Fig. 10(d)) might be attributed to GB migration. Also, some sub-micron Al_3Mg_2 precipitates along GBs are detected (as indicated by yellow arrows in Fig. 10(c) and (d)), which might precipitate during ECAP or in the early tensile stage and inevitably coarsen with tensile deformation proceeding at elevated temperature of 573 K for a long duration of 1.5 h.

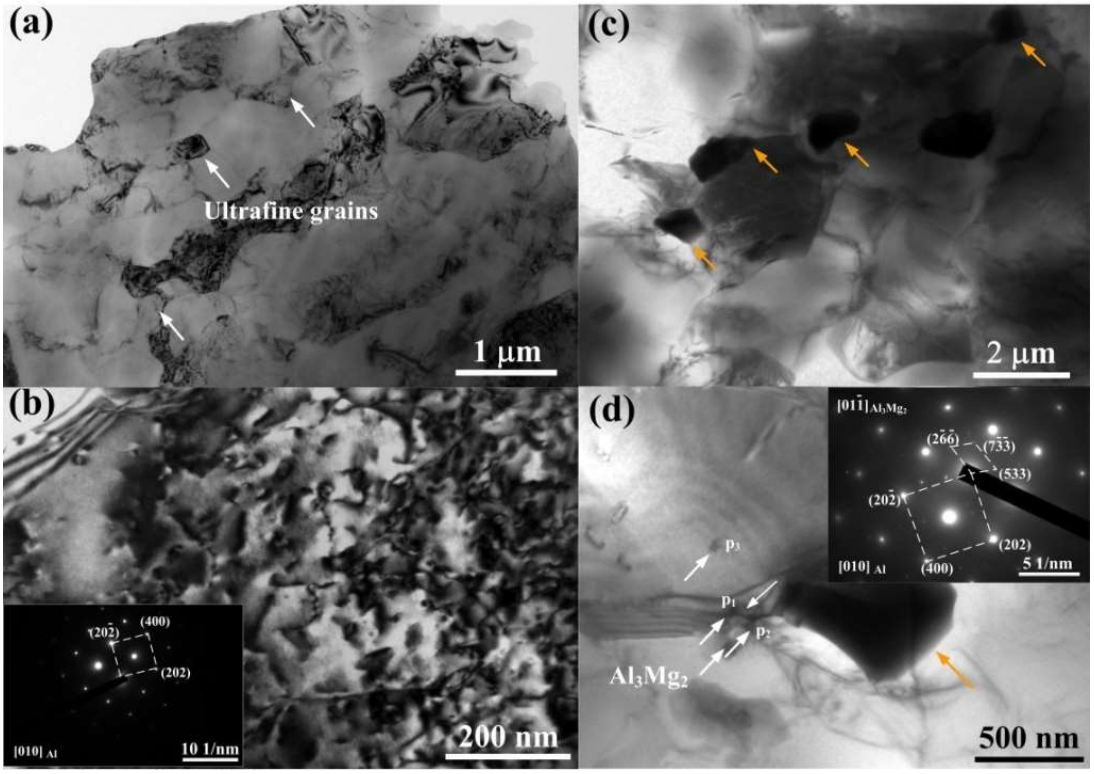

Fig. 10. TEM images of the 4P ECAPed Al–7Mg sample: (a) and (b) annealed at 573 K for 10 min as well as (c) and (d) tension fractured at 573 K and 1×10^{-3} s^{-1}. The inset in (b) is diffraction pattern; the inset in (d) is diffraction pattern corresponding to the region containing nano-sized particles.

4. Discussion

4.1. The anomalous temperature dependence of ductility, yield stress and hardening

Note that in the present Al–7Mg alloy with multi-scale microstructural heterogeneities, a high elongation to failure (~523%) is obtained at the relatively high strain rate of 1×10^{-3} s^{-1}, while lower elongations to failure, i.e. ~155–318%, are recorded at the lower strain rate of 5×10^{-4} s^{-1} at 548–623 K. This is opposite to the well-known viewpoint that a lower strain rate in general corresponds to a higher elongation to failure. It should be closely related to the microstructural evolution of the 4P Al–7Mg alloy with multi-scale microstructural heterogeneities depending on the tensile deformation parameters.

At a constant strain rate of 5×10^{-4} s^{-1}, the test temperature plays a significant role on the CDRX process and hence grain structure evolution and elongations (Fig. 7). When deformed at a low temperature of 548 K, incomplete CDRX occurs; some coarse grains containing LAGBs coexist with many fine equiaxed grains in the fractured sample (Fig. 7(a)). The retained coarse grains and the

relatively high fraction of LAGBs, i.e. 22%, suggest that mainly CDRX accommodates deformation while GBS plays a less significant role. This is consistent with the moderate elongation of ~251% and *m* value of ~0.38 (Fig. 6(c)).

In case of tensile deformation at 623 K, the evident grain growth to ~20 μm (Fig. 7(d)) does not favor GBS. In contrast, both the elevated test temperature and the large grain size decrease the threshold stress for activation of diffusional creep (Sherby and Wadsworth, 1989). Thus, diffusional creep is considered as the dominant deformation mechanism during test at 623 K, as again reflected by the relatively low *m* value of ~0.26 (Fig. 6(c)), leading to premature fracture with a lower elongation of ~155%.

In addition, abnormal behaviors of initial hardening and yield stress exist in the 4P Al–7Mg sample with increasing test temperatures. The initial hardening effect and yield stress first decreases with increasing temperature from 523 K to 573 K, but suddenly increases when tested at 623 K, leading to a higher yield stress at 623 K. Note that the observed temperature dependence of yield stress, hardening and ductility is contrary to the conventional viewpoint that increasing test temperature would decrease yield stress but increase ductility owing to decreased hardening effect originated from enhanced thermal activation. The anomalous temperature dependence of yield stress, hardening and ductility is explained in detail as described in below.

In general, the deformation behaviors of metallic materials at high temperatures can be expressed by the following equation between stress and strain rate (Ruano et al., 2003; Sherby and Burke, 1968):

$$\dot{\varepsilon} = A\frac{D}{b^2}\left(\frac{b}{d}\right)^p\left(\frac{\sigma}{E}\right)^n \quad (2)$$

where *A* is a dimensionless constant, *D* is the appropriate diffusion coefficient that controls creep, *b* is Burgers vector, *d* is grain size, *p* is grain size exponent that is positive if GBS is dominant whereas the *p* value approaches zero when dislocation creep or solute drag creep becomes dominant (Hsiao and Huang, 2002), *n* (= 1/*m*) is stress exponent and it is generally positive when alloys are subjected to tensile deformation at high temperatures (Masuda and Sato, 2020), σ is flow stress and *E* is uniaxial modulus. Eq. (2) seems to indicate that when the GB is the dominant contributor to creep deformation, flow stress (σ) at a defined strain rate is expected to increase for increasing grain size, which is inverse

to that in the Hall-Petch mechanics. In fact, upon deformation at room temperature, finer grains provide more GBs that act as obstacles for dislocation motion, which thus contributes to higher strength (Xu et al., 2020). However, when deformed at elevated temperatures, the higher area-fraction GBs provide more channels for GB diffusion and dislocation creep, accommodating GBS, accompanied with dislocations (or pile-ups) easily being absorbed into GBs (Wei et al., 2003).

When tested at 623 K, the Al–7Mg alloy exhibits rapid grain growth to ~20 μm (Fig. 7(d)). In contrast, a fine grain size of 3–5 μm maintains, i.e. higher area-fraction GBs, when tested at lower temperatures, i.e., 548 K and 573 K (Fig. 7(a–c)). Thus, the sharp increase in grain size suggests less GB diffusion and dislocation creep, leading to the yield stress at 623 K higher than that at 523 K and 573 K. Actually, a similar anomalous temperature dependence of flow stresses was reported in a Mg–9Al–1Zn alloy subjected to tensile deformation at 623 K and 673 K, exhibiting a higher flow stress in comparison to the deformation at 573 K, which was also attributed to the rapid grain coarsening beyond 573 K (Kim and Kim, 2016).

One may suspect that the solute-dislocation interaction induced DSA could be responsible partially for the anomalous increase in yield stress at 623 K. The DSA generally prevails during plastic deformation at intermediate temperatures, accompanied with oscillatory behavior of the stress-strain curve, referred to as PLC effect (Meng et al., 2019). However, the serrated flow or PLC in Al–Mg alloys would disappear when deformed at high temperatures, with positive strain rate sensitivity, *m*, obtained (Fu et al., 2012). In the present study, no serrations appear on the stress-strain curve; meanwhile the calculated results show that the 4P Al–7Mg alloy possesses a positive *m* value of ~0.26, indicating the absence of DSA. Thereby, it is believed that the solute-dislocation interaction induced DSA should not be taken into consideration for the anomalous increase in yield stress at 623 K.

4.2. Role of coarse-deformed grains underwent CDRX on coordinating hot tensile deformation process

The heterogeneous grain structure without dispersed second-phase particles, in principle, does not favor superplastic deformation according to previous research (Avtokratova et al., 2012). However, as listed in Table 1, the recorded superplasticity of ~523% elongation of the present high solid solution

Al–7Mg alloy is even higher than those of uniform-grained Al–Mg based alloys with transient elements (without Sc and/or Zr) (Masuda et al., 2018; Portnoy et al., 2013; Soer et al., 2006). For example, an Al–4.94Mg–1.53Mn alloy exhibited a fracture elongation of 320% at 723 K and 1×10^{-3} s^{-1} (Masuda et al., 2018). Similarily, an Al–6.3Mg–0.7Mn–0.3Cr alloy containing dispersed nano-sized Al_6(Mn,Cr) particles and hence a finer grain structure displayed an elongation to failure of 450% at 803 K and 5×10^{-3} s^{-1} (Portnoy et al., 2013).

EBSD analyses (Fig. 8) reveal that a large fraction of equiaxed sub-grains have formed in coarse-deformed grains of the bimodal-grained Al–7Mg alloy in the early tensile stage. Meanwhile, LAGBs in coarse grains evolve gradually into HAGBs as a consequence of continuous absorption of dislocations, implying the formation of equiaxed grains is through a CDRX process (Sun et al., 2018; Zhang et al., 2020). On one hand, CDRX in coarse-deformed grains acts as an effective mode to decrease internal strains and relieve work hardening with deformation proceeding (Fig. 8(e–h)), which is believed to play an important role on accommodating deformation strain in the early tensile stage. In fact, a similar fine equiaxed recrystallized grain structure with an average size of ~3–5 μm has formed in fractured samples undergone superplastic deformation under strain rates of 5×10^{-4} and 1×10^{-2} s^{-1} at 573 K. It suggests that 573 K is an optimum temperature to relax strain concentration via CDRX, e.g. favoring a compatible deformation process. For unimodal coarse-grained 2P Al–7Mg alloy subjected to tensile test at similar conditions, the coarse-deformed grains underwent CDRX also favor a compatible deformation at the early tensile stage. However, an inevitable rapid grain growth occurs due to the absence of effective inhibiting effect on GBs, see Fig. S1. Correspondingly, the unimodal coarse-grained 2P sample shows much lower elongations to failure when deformed at similar hot tensile conditions, see Fig. 6(a).

Moreover, the coarse-deformed grains underwent CDRX lead to the decreased stored energy and hence lower driving force for abnormal growth of pre-existing ultrafine grains in the bimodal grain structure. It has been confirmed in our previous work that static recrystallization occurs preferably in coarse-deformed grains, resulting in decreased stored energy for growth of ultrafine grains in the bimodal grain structure during static annealing treatment at moderate to high temperatures (Zha et al., 2021). It agrees well with EBSD results that no abnormal grain growth has occurred in the present

bimodal-grained Al–7Mg alloy subjected to the tensile test at 573 K (Fig. 8). Eventually, a uniform fine-grained structure forms and maintains during the long-time tensile deformation (~1.5 h) at 573 K (Fig. 8(a–d)), in favorable for superplasticity.

4.3. Role of Mg solute segregation on thermal stability during hot tensile deformation

It has been reported that Mg concentrations above 5 wt.% can easily give rise to dynamic recrystallization (DRX) within a certain domain of temperature and strain rate, which in the absence of second-phase particles leads to rapid coarsening of the microstructure (Soer et al., 2006). To invetigate the grain coarsening kinetics in the present high solid solution Al–7Mg alloy, the average recrystallized grain size as a function of time during tensile deformation at 573 K and 1×10^{-3} s^{-1} is plotted in Fig. 11(a). The grain growth kinetics at a constant temperature can be expressed as (Peng et al., 2017):

$$d^n - d_0^n = kt \quad (3)$$

where n is the grain growth exponent, d is the instantaneous average grain size at time t, d_0 is the initial grain size, and k is the parameter representing the mobility of GBs and interface. Here, the effect of stored energy on grain growth is ignored as nearly all fine recrystallized grains are free of internal strains during tension at 573 K and 1×10^{-3} s^{-1} (Fig. 8(e–h)). Therefore, the discussed n here is based on the assumption that GB curvature is the driving force for GB migration (Peng et al., 2017). In general, the larger the n value, the slower the grain growth rate is, indicating higher thermal stability. When d_0 can be neglected compared with d, $\ln d$ is a linear function of $\ln t$ with a slope equal to $1/n$. The estimated n value for the 4P Al–7Mg alloy is ~4.1 (Fig. 11(b)), which is apparently larger than that of ~2 estimated for pure metals or alloys annealed at very high temperatures (Roy et al., 2006).

To determine the driving force required for the initiation of grain growth (Dhal et al., 2015), activation energy for GB mobility, Q was calculated based on the following exponential relationship (Roy et al., 2006):

$$d^n - d_0^n = k_0 t exp(-\frac{Q}{RT}) \quad (4)$$

where k_0 is a constant independent of temperature and time, R is the gas constant and T is the annealing temperature. As reported by Zhou *et al*., when Q was determined in a temperature zone, the n value should be independent of temperature (Zhou et al., 2011). Here, the n value of ~4.1 at 573 K could roughly represent the average n value in the low temperature zone (523–573 K) for the 4P sample. Note that d values used in Eq. (3) are selected from samples after an elongation of ~200% under three studied tensile test temperatures at 1×10^{-3} s^{-1}, i.e. 523, 548 and 573 K (see Fig. S3). According to the plot of $\ln(d^n-d_0^n)$ versus $1000/T$ derived from the grain structure evolution during tensile deformation (Fig. 11(c)), the Q value in the temperature zone of 523–573 K of the 4P Al–7Mg sample is ~47 kJ/mol. It is much lower than that of the GB self-diffusion for pure Al (~86 kJ/mol) (Roy et al., 2006) and the diffusion of Mg atoms in the Al matrix (~130.5 kJ/mol) (Wang, 1996). In general, the enhanced migration of non-equilibrium GBs of SPD-proceesed alloys results in low additional driving force requied for GBs being rearranged and hence lower Q values (Roy et al., 2006). Compared with ~30 kJ/mol at < 548 K in a dilute Al–3Mg alloy processed by ECAP (Wang, 1996), the higher Q value of ~47 kJ/mol obtained under tensile deformation at ≤ 573 K reflects enhanced thermal stability in the present 4P Al–7Mg alloy with multi-scale microstructural heterogeneities. It should be mainly attributed to the strong Mg solute segregation in the latter (Fig. 5), stabilizing non-equilibrium GBs, which thus restricts the rearrangement of GBs to some extent.

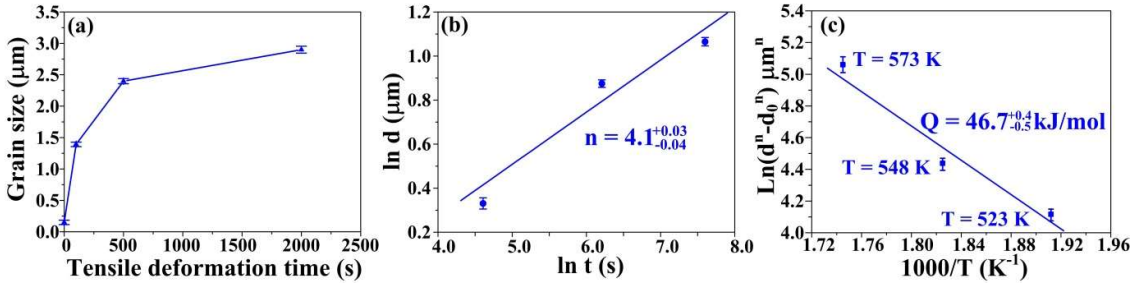

Fig. 11. (a) The plot of grain size versus tensile deformation time, (b) the plot of ln d versus ln t derived from the grain strucutre evolution during tensile deformation at 573 K and (c) the plot of $\ln(d^n-d_0^n)$ versus $1000/T$ derived from the grain strucutre evolution during tensile deformation in the temperature zone of 523–573 K for the 4P ECAPed Al–7Mg sample. The error bars in (a) represent a standard deviation of grain size measurements of each sample; the error bars in (b) and (c) correspond to the uncertainty of grain size measurements.

Thermodynamically, the free energy of GBs can be decreased by solute segregation, reducing the driving force for recrystallization and grain coarsening, enabling stabilization of nano/ultrafine grains (Chookajorn et al., 2012). Specifically, recent work has reported that Mg segregation along GBs can

reduce GB energy and hence the driving force for grain growth in nanocrystalline Al–5Mg and Al–10Mg alloys (Devaraj et al., 2019). Kinetically, GB motion can be restricted by either solute segregation through dragging effect or nanoscale precipitates at GBs (Gwalani et al., 2019; Kalidindi and Schuh, 2017). Thereby, Mg solute segregation along GBs contributes to enhanced thermal stability of ultrafine grains in the present 4P Al–7Mg alloy, preventing abnormal grain growth especially in the early stage of hot tensile deformation. Moreover, the high-content solute Mg atoms in the matrix can effectively restrain dislocation motion and retard the recrystallization process, accompanying with delayed grain coarsening (Tang et al., 2020). Recently, the impact of Mg segregation on GB diffusion of both alloy components in Al–Mg alloys has been predicted based on atomistic computer simulations, which suggests that Mg segregation can significantly reduce the rate of mass transport along GBs in Al–Mg alloys (Koju and Mishin, 2020). Thereby, the reduced atomic mobility can be responsible for the improved stability of the microstructure at elevated temperatures. In addition, the Al_3Mg_2 precipitates are expected to delay grain growth to some degree in the late stage of superplastic deformation, though the low number density suggests a minor effect on retarding the migration of dislocations and GBs (Huang et al., 2018).

As a result, the bimodal grain structure gradually transforms into a uniform fine one with only slight grain growth during the long-time tensile deformation (~1.5 h) at 573 K and 1×10^{-3} s^{-1} (Fig. 8(a–d)), indicative of high thermal stability of the present high solid solution Al–7Mg alloy. In contrast, coarsening of ultrafine grains has been frequently observed in SPD-processed dilute Al–Mg alloys with Mg contents ≤ 3 wt.% upon static annealing at moderate to high temperatures (Meng et al., 2019). It is thus believed that the microstructural heterogeneities, including the bimodal grain structure and strong Mg solute segregation, as well as their evolutions subjected to tensile deformation at a selected temperature and strain rate together enable a stable uniform fine grain structure in the present high solid solution Al–7Mg alloy.

4.4. High superplasticity cooperated by CDRX and GBS

The present high solid solution Al–7Mg alloy with multi-scale microstructural heterogeneities exhibits superplasticity of ~523% elongation at the optimal tensile condition of 573 K and 1×10^{-3} s^{-1},

which is much higher than previously reported single-phase uniform-grained Al–Mg alloys. This is partially attributed to the accommodated dislocation motion by CDRX occurred in those coarse-deformed grains in the early tensile stage. Despite the CDRX was revealed during hot tensile deformation at all tested strains in the range of 5×10^{-4} s^{-1}–1×10^{-2} s^{-1}, the deformation at higher strain rate provides more intergranular strain and more pronounced DRX effect, which keeps more refined grains even at larger strains. In fact, DRX, as an alternative way of tailoring grain structure, plays an important role on preparing metallic materials with high performance (P. Zhao et al., 2018). It was reported that dynamic reconstruction, including grain refinement, in some coarse-grained and band-grained alloys by DRX could result in enhanced ductility or even superplasticity (300–700%) during hot tensile deformation (Jia et al., 2019; Li et al., 2017).

Many studies indicate that solute Mg atoms greatly influence the deformation mechanisms and thus ductility/superplasticity at elevated temperatures of Al alloys. Qiao et al. found that an increase of Mg content led to decreased stress exponent, i.e. increased *m* value, in Al–*x*Mg–5Zn alloys, indicating higher elongation could be obtained (Qiao, 2003). Also, superplasticity was achieved in a high-solute Mg AA5083 alloy rather than in low-solute Mg AA3003, which was attributed to an enhancement of Al self-diffusion by high-content Mg atoms, promoting diffusion creep (Sotoudeh and Bate, 2010). In a recent study, it reported that the Mg GB segregation significantly reduced the rate of mass transport along GBs in Al–Mg alloys and retarded atomic mobility (Koju and Mishin, 2020), which restricts GB migration in fine-grained regions. The reduced GBS contribution partially originated from the inhibited GB mobility by Mg segregation in an Al–3.9Zn–4.1Mg–0.8Cu–2.8Ni–0.25Zr alloy was also reported in a experemental work (Yakovtseva et al., 2020). Therefore, by acting in a similar way as nano-sized precipitates (Cepeda-Jiménez et al., 2017), the Mg segregation along GBs should result in the decreased contribution of GBS to total strain in the early stage of superplastic deformation. Nevertheless, the Mg segregation along GBs plays a critical role on stabilizing fine grains and restricting abnormal grain growth. The uniform grain growth, as a necessary condition for achieving superplasticity, favors good compatibility of plastic deformation, which can minimize void formation and coalescence in fine-grained regions in the early stage of superplastic deformation (Kaibyshev et al., 2005). Note that in the present Al–7Mg alloy with a heterogeneous grain structure, the GBS only takes

a dominant role at the later deformation stage when the tensile elongation is ≥ 300%. It is believed that the major part of solute Mg is being in solid solution after exposure to the elevated temperature for such a long duration. In summary of the above, the presence of Mg does not hamper the superplasticity deformation of present Al–7Mg alloy with a heterogeneous grain structure.

With increasing elongations ≥ 300%, the randomly distributed texture with a very low intensity and a low internal strain reflect the increased contribution from GBS. It agrees well with the corresponding calculated m value ≥ 0.48 at 573 K (Fig. 6(c)), close to that of the onset of GBS. The calculated Q value of ~78 kJ/mol, approaching to that of GB self-diffusion of Al alloys, i.e. 86 kJ/mol (Kawasaki et al., 2011), confirms that the cooperative process between GBS and GB diffusion, which plays straining and accommodating roles, respectively (Masuda and Sato, 2020), during superplastic deformation. Furthermore, the well-kept uniform fine grain structure (< 5 μm) bounded mainly by HAGBs in the late tensile stage (~300–523%) favors the stable GBS proceeding.

Above analyses suggest that the deformation mechanism changes from dislocation motion accommodated by CDRX in the early tensile stage to GBS-dominant in the late tensile stage. It is ascribed mainly to the formation of a uniform fine grain structure, which is well kept though subjected to the long-time tensile deformation at the elevated temperature. Inspired by aforementioned results, it is believed that high solid solution Al alloys with multi-scale microstructural heterogeneities could achieve high superplasticity under proper tensile test conditions, where CDRX could occur in coarse-deformed grains while the ultrafine grains are kept from abnormal growth. This challenges current understanding that superplastic Al alloys usually require a uniform fine grain structure containing well-dispersed particles in the starting microstructure.

5. Conclusions

The present work reveals that the high solid solution Al–7Mg alloy with multi-scale microstructural heterogeneities, i.e. a bimodal grain structure coupling with Mg solute segregation along GBs, exhibits notable superplasticity of ~523% at 573 K and a relatively high strain rate of 1×10^{-3} s^{-1}. However, the benefit of the bimodal grain structure on superplastic deformation is lost at higher tensile deformation temperatures (e.g. at 623 K). To reveal the underlying mechanisms, we

systematically studied the evolution of bimodal grain structure, solute Mg distribution and their effects on superplastic deformation behaviors by EBSD, TEM-ASTAR, APT and TEM analyses. The following conclusions can be drawn:

(i) At the optimal deformation condition for superplastic deformation, i.e., 573 K and 1×10^{-3} s^{-1}, the evolution of bimodal grain structure plays a significant role on coordinating the hot tensile deformation process. Especially, the early tensile stage is accommodated by CDRX occurring in coarse-deformed grains feasuring high stored energy, which relaxes strain concentration. Moreover, the preferred occurrence of CDRX in coarse-deformed grains decreases stored energy and hence driving force for rapid coarsening of pre-existing nano/ultrafine grains.

(ii) The pronounced Mg solute segregation along GBs of nano/ultrafine grains in the initial bimodal grain structure improves their coarsening resistance by decreasing both GB energy and GB mobility. In addition, nano-sized and sub-micron Al_3Mg_2 precipitates are expected to restrict the migration of dislocations and GBs, which hence delays the complete recrystallization time and restrains grain growth.

(iii) A uniform fine equiaxed grain structure forms after ~300% elongation, replacing the initial bimodal grain structure, with an average grain size of ~3.6 μm maintaining till fracture during deformation at 573 K and 1×10^{-3} s^{-1}. Thereby, in the late deformation stage, GBS takes the dominant role and is responsible for the impressive superplasticity, as reflected by the randomized texture with sharply reduced intensity and the high *m* value of ~0.75. The calculated deformation activation energy of ~78 kJ/mol, close to that of GB self-diffusion of Al alloys, also confirms the occurrence of GB diffusion-controlled GBS.

(iv) The temperature plays a significant role on hot deformation behaviours of present Al–7Mg alloy with multi-scale microstructural heterogeneities. During deformation above a certain temperature, e.g. at 623 K, remarkable grain growth occurs and the average grain size reaches ~20 μm, which does not favor GBS (a low *m* value of ~0.26), leading to a low elongation to failure of ~155%. Also, when deformed at a low temperature (e.g. at 548 K), mainly incomplete CDRX accommodates deformation while GBS plays a less significant role (a moderate *m* value of ~0.38), which corresponds to low superplasticity of ~251%.

(v) This study demonstrates the possibility of achieving superplasticity in a high solid solution Al–7Mg alloy with multi-scale microstructural heterogeneities. The obtained results challenge the current understanding that superplastic deformation requires a multiphase structure or a uniform fine grain structure with dispersoids. The present work gives a new direction for designing bulk metallic materials with multi-scale microstructural heterogeneities for superplastic processing.

Acknowledgements

Financial supports from The Natural Science Foundation of China (Nos. 51922048, 51625402 and 51790483) are greatly acknowledged. Partial financial support came from the Fundamental Research Funds for the Central Universities, JLU, Program for JLU Science and Technology Innovative Research Team (JLUSTIRT, 2017TD-09).

Nomenclature

ECAP	equal-channel angular pressing
GBs	grain boundaries
EBSD	electron backscatter diffraction
TEM	transmission electron microscopy
APT	atom probe tomography
CDRX	continuous dynamic recrystallization
GBS	grain boundary sliding
GB	grain boundary
PLC	Portevin-Le Chatelier
SPF	superplastic forming
SPD	severe plastic deformation
FSP	friction stir processing
HPT	high-pressure torsion
DSA	dynamic strain aging
SEM	scanning electron microscopy
ED	extrusion direction
LAGBs	low-angle grain boundaries
KAM	kernel average misorientation
HAGBs	high-angle grain boundaries
IPF	inverse pole figure
SAD	selected area diffraction

HAADF	high-angle annular dark field
STEM	scanning transmission electron microscopy
XRD	X-ray diffraction
$\dot{\varepsilon}$	strain rate (Eq. (1))
A	constant of material (Eq. (1))
σ	flow stress (Eq. (1))
R	gas constant (Eq. (1))
T	temperature (Eq. (1))
Q	deformation activation energy (Eq. (1))
A	dimensionless constant (Eq. (2))
D	appropriate diffusion coefficient (Eq. (2))
b	Burgers vector (Eq. (2))
d	grain size (Eq. (2))
p	grain size exponent (Eq. (2))
n	stress exponent (Eq. (2))
E	uniaxial modulus (Eq. (2))
n	grain growth exponent (Eq. (3))
d	instantaneous average grain size at time t (Eq. (3))
d_0	initial grain size (Eq. (3))
k	parameter representing the mobility of GBs and interface (Eq. (3))
Q	activation energy for GB mobility (Eq. (4))
k_0	constant independent of temperature and time (Eq. (4))

References

Avtokratova, E., Sitdikov, O., Markushev, M., Mulyukov, R., 2012. Extraordinary high-strain rate superplasticity of severely deformed Al-Mg-Sc-Zr alloy. Mater. Sci. Eng. A 538, 386–390. https://doi.org/10.1016/j.msea.2012.01.041

Bobylev, S. V., Enikeev, N.A., Sheinerman, A.G., Valiev, R.Z., 2019. Strength enhancement induced by grain boundary solute segregations in ultrafine-grained alloys. Int. J. Plast. 123, 133–144. https://doi.org/10.1016/j.ijplas.2019.07.013

Bussiba, A., Ben Artzy, A., Shtechman, A., Ifergan, S., Kupiec, M., 2001. Grain refinement of AZ31 and ZK60 Mg alloys-Towards superplasticity studies. Mater. Sci. Eng. A 302, 56–62. https://doi.org/10.1016/S0921-5093(00)01354-X

Cepeda-Jiménez, C.M., Castillo-Rodríguez, M., Molina-Aldareguia, J.M., Huang, Y., Langdon, T.G., Pérez-Prado, M.T., 2017. Controlling the high temperature mechanical behavior of Al alloys by precipitation and severe straining. Mater. Sci. Eng. A 679, 36–47. https://doi.org/10.1016/j.msea.2016.10.026

Chookajorn, T., Murdoch, H.A., Schuh, C.A., 2012. Design of stable nanocrystalline alloys. Science 337, 951–954. https://doi.org/10.1126/science.1224737

Chuvil, V.N., Gryaznov, M.Y., Shotin, S. V, Kopylov, V.I., Nokhrin, A. V, Likhnitskii, C. V, Murashov, A.A., Bobrov, A.A., Tabachkova, N.Y., Pirozhnikova, O.E., 2021. Investigation of superplasticity and dynamic grain growth in ultrafine-grained Al–0.5%Mg–Sc alloys. J. Alloys Compd. 877, 160099. https://doi.org/10.1016/j.jallcom.2021.160099

Devaraj, A., Wang, W., Vemuri, R., Kovarik, L., Jiang, X., Bowden, M., Trelewicz, J.R., Mathaudhu, S., Rohatgi, A., 2019. Grain boundary segregation and intermetallic precipitation in coarsening resistant nanocrystalline aluminum alloys. Acta Mater. 165, 698–708. https://doi.org/10.1016/j.actamat.2018.09.038

Dhal, A., Panigrahi, S.K., Shunmugam, M.S., 2015. Precipitation phenomena, thermal stability and grain growth kinetics in an ultra-fine grained Al 2014 alloy after annealing treatment. J. Alloys Compd. 649, 229–238. https://doi.org/10.1016/j.jallcom.2015.07.098

Duan, Y., Xu, G., Tang, L., Liu, Y., Xu, J., Deng, Y., Yin, Z., 2017. Excellent high strain rate superplasticity of Al-Mg-Sc-Zr alloy sheet produced by an improved asymmetrical rolling process. J. Alloys Compd. 715, 311–321. https://doi.org/10.1016/j.jallcom.2017.04.273

Fu, S., Cheng, T., Zhang, Q., Hu, Q., Cao, P., 2012. Two mechanisms for the normal and inverse behaviors of the critical strain for the Portevin-Le Chatelier effect. Acta Mater. 60, 6650–6656. https://doi.org/10.1016/j.actamat.2012.08.035

Garner, A., Euesden, R., Yao, Y., Aboura, Y., Zhao, H., Donoghue, J., Curioni, M., Gault, B., Shanthraj, P., Barrett, Z., Engel, C., Burnett, T.L., Prangnell, P.B., 2021. Multiscale analysis of grain boundary microstructure in high strength 7xxx Al alloys. Acta Mater. 202, 190–210. https://doi.org/10.1016/j.actamat.2020.10.021

Geng, R., Zhao, Q., Qiu, F., Jiang, Q., 2020. Simultaneously increased strength and ductility via the hierarchically heterogeneous structure of Al-Mg-Si alloys/nanocomposite. Mater. Res. Lett. 8, 225–231. https://doi.org/10.1080/21663831.2020.1744759

Gwalani, B., Salloom, R., Alam, T., Valentin, S.G., Zhou, X., Thompson, G., Srinivasan, S.G., Banerjee, R., 2019. Composition-dependent apparent activation-energy and sluggish grain-growth in high entropy alloys. Mater. Res. Lett. 7, 267–274. https://doi.org/10.1080/21663831.2019.1601644

Hsiao, I.C., Huang, J.C., 2002. Deformation Mechanisms during Low- and High- Temperature Superplasticity in 5083 Al-Mg Alloy. Metall. Mater. Trans. A 33, 1373–1384. https://doi.org/10.1007/s11661-002-0062-0

Huang, K., Marthinsen, K., Zhao, Q., Logé, R.E., 2018. The double-edge effect of second-phase particles on the recrystallization behaviour and associated mechanical properties of metallic materials. Prog. Mater. Sci. 92, 284–359. https://doi.org/10.1016/j.pmatsci.2017.10.004

Jang, D.H., Park, Y.B., Kim, W.J., 2019. Significant strengthening in superlight Al-Mg alloy with an exceptionally large amount of Mg (13 wt.%) after cold rolling. Mater. Sci. Eng. A 744, 36–44. https://doi.org/10.1016/j.msea.2018.11.132

Jia, L., Ren, X., Hou, H., Zhang, Y., 2019. Microstructural evolution and superplastic deformation mechanisms of as-rolled 2A97 alloy at low-temperature. Mater. Sci. Eng. A 759, 19–29. https://doi.org/10.1016/j.msea.2019.04.102

Jobba, M., Mishra, R.K., Niewczas, M., 2015. Flow stress and work-hardening behaviour of Al-Mg binary alloys. Int. J. Plast. 65, 43–60. https://doi.org/10.1016/j.ijplas.2014.08.006

Kabirian, F., Khan, A.S., Pandey, A., 2014. Negative to positive strain rate sensitivity in 5xxx series aluminum alloys: Experiment and constitutive modeling. Int. J. Plast. 55, 232–246. https://doi.org/10.1016/j.ijplas.2013.11.001

Kaibyshev, R., Shipilova, K., Musin, F., Motohashi, Y., 2005. Achieving high strain rate superplasticity in an Al-Li-Mg alloy through equal channel angular extrusion. Mater. Sci. Technol. 21, 408–418. https://doi.org/10.1179/174328405X36610

Kalidindi, A.R., Schuh, C.A., 2017. Stability criteria for nanocrystalline alloys. Acta Mater. 132, 128–137. https://doi.org/10.1016/j.actamat.2017.03.029

Kawasaki, M., Balasubramanian, N., Langdon, T.G., 2011. Flow mechanisms in ultrafine-grained metals with an emphasis on superplasticity. Mater. Sci. Eng. A 528, 6624–6629. https://doi.org/10.1016/j.msea.2011.05.005

Kim, B., Kim, J.C., Lee, S., Lee, K.S., Lee, J.G., Park, S.S., 2017. High-strain-rate superplasticity of fine-grained Mg–6Zn–0.5Zr alloy subjected to low-temperature indirect extrusion. Scr. Mater. 141, 138–142. https://doi.org/10.1016/j.scriptamat.2017.08.008

Kim, Y.S., Kim, W.J., 2016. Microstructure and superplasticity of the as-cast Mg-9Al-1Zn magnesium alloy after high-ratio differential speed rolling. Mater. Sci. Eng. A 677, 332–339. https://doi.org/10.1016/j.msea.2016.09.063

Koju, R.K., Mishin, Y., 2020. Atomistic study of grain-boundary segregation and grain-boundary diffusion in Al-Mg alloys. Acta Mater. 201, 596–603. https://doi.org/10.1016/j.actamat.2020.10.029

Komura, S., Horita, Z., Furukawa, M., Nemoto, M., Langdon, T.G., 2001. An evaluation of the flow behavior during high strain rate superplasticity in an al-mg-sc alloy. Metall. Mater. Trans. A Phys. Metall. Mater. Sci. 32, 707–716. https://doi.org/10.1007/s11661-001-1006-9

Li, J., Chen, S., Weng, G.J., Lu, W., 2021. A micromechanical model for heterogeneous nanograined metals with shape effect of inclusions and geometrically necessary dislocation pileups at the domain boundary. Int. J. Plast. 144, 103024. https://doi.org/10.1016/j.ijplas.2021.103024

Li, M., Pan, Q., Shi, Y., Sun, X., Xiang, H., 2017. High strain rate superplasticity in an Al–Mg–Sc–Zr alloy processed via simple rolling. Mater. Sci. Eng. A 687, 298–305. https://doi.org/10.1016/j.msea.2017.01.091

Li, S., Li, Y., Lo, Y.C., Neeraj, T., Srinivasan, R., Ding, X., Sun, J., Qi, L., Gumbsch, P., Li, J., 2015. The interaction of dislocations and hydrogen-vacancy complexes and its importance for deformation-induced proto nano-voids formation in α-Fe. Int. J. Plast. 74, 175–191. https://doi.org/10.1016/j.ijplas.2015.05.017

Li, X., Xia, W., Chen, J., Yan, H., Li, Z., Su, B., Song, M., 2021. Bimodal-Structured Al–Mg Alloy with High Strength and Ductility Processed by High Strain Rate Rolling at Medium Temperature. Met. Mater. Int. https://doi.org/10.1007/s12540-020-00929-w

Liu, X., Ye, L., Tang, J., Shan, Z., Ke, B., Dong, Y., Chen, J., 2020. Superplastic deformation mechanisms of an Al–Mg–Li alloy with banded microstructures. Mater. Sci. Eng. A 805, 140545. https://doi.org/10.1016/j.msea.2020.140545

Liu, Y., Liu, M., Chen, X., Cao, Y., Roven, H.J., Murashkin, M., Valiev, R.Z., Zhou, H., 2019. Effect of Mg on microstructure and mechanical properties of Al-Mg alloys produced by high pressure torsion. Scr. Mater. 159, 137–141. https://doi.org/10.1016/j.scriptamat.2018.09.033

Malopheyev, S., Mironov, S., Vysotskiy, I., Kaibyshev, R., 2016. Superplasticity of friction-stir welded Al-Mg-Sc sheets with ultrafine-grained microstructure. Mater. Sci. Eng. A 649, 85–92. https://doi.org/10.1016/j.msea.2015.09.106

Masuda, H., Kanazawa, T., Tobe, H., Sato, E., 2018. Dynamic anisotropic grain growth during superplasticity in Al–Mg–Mn alloy. Scr. Mater. 149, 84–87. https://doi.org/10.1016/j.scriptamat.2018.02.021

Masuda, H., Sato, E., 2020. Diffusional and dislocation accommodation mechanisms in superplastic materials. Acta Mater. 197, 235–252. https://doi.org/10.1016/j.actamat.2020.07.042

Meng, C., Hu, W., Sandlöbes, S., Korte-Kerzel, S., Gottstein, G., 2019. The effect of large plastic deformation on elevated temperature mechanical behavior of dynamic strain aging Al-Mg alloys. Acta Mater. 181, 67–77. https://doi.org/10.1016/j.actamat.2019.09.024

Mikhaylovskaya, A. V., Kotov, A.D., Pozdniakov, A. V., Portnoy, V.K., 2014. A high-strength aluminium-based alloy with advanced superplasticity. J. Alloys Compd. 599, 139–144. https://doi.org/10.1016/j.jallcom.2014.02.061

Ovid'ko, I.A., Valiev, R.Z., Zhu, Y.T., 2018. Review on superior strength and enhanced ductility of metallic nanomaterials. Prog. Mater. Sci. 94, 462–540. https://doi.org/10.1016/j.pmatsci.2018.02.002

Pandey, A., Khan, A.S., Kim, E.Y., Choi, S.H., Gnäupel-Herold, T., 2013. Experimental and numerical investigations of yield surface, texture, and deformation mechanisms in AA5754 over low to high temperatures and strain rates. Int. J. Plast. 41, 165–188. https://doi.org/10.1016/j.ijplas.2012.09.006

Peng, H.R., Gong, M.M., Chen, Y.Z., Liu, F., 2017. Thermal stability of nanocrystalline materials: thermodynamics and kinetics. Int. Mater. Rev. 62, 303–333. https://doi.org/10.1080/09506608.2016.1257536

Peng, J., Bahl, S., Shyam, A., Haynes, J.A., Shin, D., 2020. Solute-vacancy clustering in aluminum. Acta Mater. 196, 747–758. https://doi.org/10.1016/j.actamat.2020.06.062

Portnoy, V.K., Rylov, D.S., Levchenko, V.S., Mikhaylovskaya, A. V, 2013. The influence of chromium on the structure and superplasticity of Al–Mg–Mn alloys. J. Alloys Compd. 581, 313–317. https://doi.org/10.1016/j.jallcom.2013.07.075

Qiao, J., 2003. The effects of ternary alloying additions on solute-drag creep in Al-Mg alloys. The University of Texas at Austin.

Reyne, B., Moes, N., Manach, P.Y., 2020. A persistent modal plastic model for instabilities in Al-Mg alloys with 1D application. Int. J. Plast. 131, 102713. https://doi.org/10.1016/j.ijplas.2020.102713

Roy, I., Chauhan, M., Lavernia, E.J., 2006. Thermal Stability in Bulk Cryomilled Ultrafine-Grained 5083 Al Alloy. Metall. Mater. Trans. A 37, 721–730. https://doi.org/10.1007/s11661-006-0044-8

Ruano, O.A., Wadsworth, J., Sherby, O.D., 2003. Deformation of fine-grained alumina by grain boundary sliding accommodated by slip. Acta Mater. 51, 3617–3634. https://doi.org/10.1016/S1359-6454(03)00180-0

Sauvage, X., Enikeev, N., Valiev, R., Nasedkina, Y., Murashkin, M., 2014. Atomic-scale analysis of the segregation and precipitation mechanisms in a severely deformed Al-Mg alloy. Acta Mater. 72, 125–136. https://doi.org/10.1016/j.actamat.2014.03.033

Sauvage, X., Wilde, G., Divinski, S. V., Horita, Z., Valiev, R.Z., 2012. Grain boundaries in ultrafine grained materials processed by severe plastic deformation and related phenomena. Mater. Sci. Eng. A 540, 1–12. https://doi.org/10.1016/j.msea.2012.01.080

Sherby, O.D., Burke, P.M., 1968. Mechanical Behavior of Crystalline Solids at Elevated Temperature. Prog. Mater. Sci. 13, 323–390. https://doi.org/10.1016/0079-6425(68)90024-8

Sherby, O.D., Wadsworth, J., 1989. Superplasticity-Recent advances and future directions. Prog. Mater. Sci. 33, 169–221. https://doi.org/10.1016/0079-6425(89)90004-2

Soer, W.A., Chezan, A.R., Hosson, J.T.M. De, 2006. Deformation and reconstruction mechanisms in coarse-grained superplastic Al–Mg alloys. Acta Mater. 54, 3827–3833. https://doi.org/10.1016/j.actamat.2006.04.014

Sotoudeh, K., Bate, P.S., 2010. Diffusion creep and superplasticity in aluminium alloys. Acta Mater. 58, 1909–1920. https://doi.org/10.1016/j.actamat.2009.11.034

Sun, Z.C., Wu, H.L., Cao, J., Yin, Z.K., 2018. Modeling of continuous dynamic recrystallization of Al-Zn-Cu-Mg alloy during hot deformation based on the internal-state-variable (ISV) method. Int. J. Plast. 106, 73–87. https://doi.org/10.1016/j.ijplas.2018.03.002

Tang, J., Jiang, F., Luo, C., Bo, G., Chen, K., Teng, J., Fu, D., Zhang, H., 2020. Integrated physically based modeling for the multiple static softening mechanisms following multi-stage hot deformation in Al-Zn-Mg-Cu alloys. Int. J. Plast. 134, 102809. https://doi.org/10.1016/j.ijplas.2020.102809

Tugcu, K., Sha, G., Liao, X.Z., Trimby, P., Xia, J.H., Murashkin, M.Y., Xie, Y., Valiev, R.Z., Ringer, S.P., 2012. Enhanced grain refinement of an Al-Mg-Si alloy by high-pressure torsion processing at 100 °C. Mater. Sci. Eng. A 552, 415–418. https://doi.org/10.1016/j.msea.2012.05.063

Wang, J., 1996. AN INVESTIGATION OF MICROSTRUCTURAL STABILITY IN AN Al-Mg ALLOY WITH SUBMICROMETER GRAIN SIZE. Acta Mater. 44, 2973–2982. https://doi.org/10.1016/1359-6454(95)00395-9

Wang, X., Li, J., Cazes, F., Hocini, A., Dirras, G., 2020. Numerical modeling on strengthening mechanisms of the harmonic structured design on CP-Ti and Ti-6Al-4V. Int. J. Plast. 133, 102793. https://doi.org/10.1016/j.ijplas.2020.102793

Wei, Y.H., Wang, Q.D., Zhu, Y.P., Zhou, H.T., Ding, W.J., Chino, Y., Mabuchi, M., 2003. Superplasticity and grain boundary sliding in rolled AZ91 magnesium alloy at high strain rates. Mater. Sci. Eng. A 360, 107–115. https://doi.org/0.1016/S0921-5093(03)00407-6

Xu, W., Liu, X.C., Li, X.Y., Lu, K., 2020. Deformation induced grain boundary segregation in nanolaminated Al–Cu alloy. Acta Mater. 182, 207–214. https://doi.org/10.1016/j.actamat.2019.10.036

Yakovtseva, O.A., Sitkina, M.N., Kotov, A.D., Rofman, O. V., Mikhaylovskaya, A. V., 2020. Experimental study of the superplastic deformation mechanisms of high-strength aluminum-based alloy. Mater. Sci. Eng. A 788, 139639. https://doi.org/10.1016/j.msea.2020.139639

Yang, C., Zhang, P., Shao, D., Wang, R.H., Cao, L.F., Zhang, J.Y., Liu, G., Chen, B.A., Sun, J., 2016. The influence of Sc solute partitioning on the microalloying effect and mechanical properties of Al-Cu alloys with minor Sc addition. Acta Mater. 119, 68–79. https://doi.org/10.1016/j.actamat.2016.08.013

Zha, M., Li, Y., Mathiesen, R.H., Bjørge, R., Roven, H.J., 2015a. Microstructure evolution and mechanical behavior of a binary Al-7Mg alloy processed by equal-channel angular pressing. Acta Mater. 84, 42–54. https://doi.org/10.1016/j.actamat.2014.10.025

Zha, M., Li, Y., Mathiesen, R.H., Bjørge, R., Roven, H.J., 2014. Achieve high ductility and strength in an Al-Mg alloy by severe plastic deformation combined with inter-pass annealing. Mater. Sci. Eng. A 598, 141–146. https://doi.org/10.1016/j.msea.2013.12.103

Zha, M., Li, Y., Mathiesen, R.H., Roven, H.J., 2015b. High ductility bulk nanostructured Al–Mg binary alloy processed by equal channel angular pressing and inter-pass annealing. Scr. Mater. 105, 22–25. https://doi.org/10.1016/j.scriptamat.2015.04.018

Zha, M., Meng, X., Zhang, H., Yin, H., Zhang, Q., Wang, C., Wang, Y., Jiang, Q., 2019. Enhancing Thermal Stability of Binary Al-Mg Alloys by Tailoring Grain Orientations Using a High Solute Mg Content. Metall. Mater. Trans. A 50, 5264–5270. https://doi.org/10.1007/s11661-019-05404-9

Zha, M., Zhang, H.M., Meng, X.T., Jia, H.L., Jin, S.B., Sha, G., Wang, H.Y., Li, Y.J., Roven, H.J., 2021. Stabilizing a severely deformed Al–7Mg alloy with a multimodal grain structure via Mg solute segregation. J. Mater. Sci. Technol. 89, 141–149. https://doi.org/10.1016/j.jmst.2021.01.086

Zha, M., Zhang, H.M., Yu, Z.Y., Zhang, X.H., Meng, X.T., Wang, H.Y., Jiang, Q.C., 2018. Bimodal microstructure–A feasible strategy for high-strength and ductile metallic materials. J. Mater. Sci. Technol. 34, 257–264. https://doi.org/10.1016/j.jmst.2017.11.018

Zhang, H.K., Xiao, H., Fang, X.W., Zhang, Q., Logé, R.E., Huang, K., 2020. A critical assessment of experimental investigation of dynamic recrystallization of metallic materials. Mater. Des. 193, 108873. https://doi.org/10.1016/j.matdes.2020.108873

Zhang, Y., Jin, S., Trimby, P.W., Liao, X., Murashkin, M.Y., Valiev, R.Z., Liu, J., Cairney, J.M., Ringer, S.P., Sha, G., 2019. Dynamic precipitation, segregation and strengthening of an Al-Zn-Mg-Cu alloy (AA7075) processed by high-pressure torsion. Acta Mater. 162, 19–32. https://doi.org/10.1016/j.actamat.2018.09.060

Zhao, D., Løvvik, O.M., Marthinsen, K., Li, Y., 2018. Segregation of Mg, Cu and their effects on the strength of Al Σ5 (210)[001] symmetrical tilt grain boundary. Acta Mater. 145, 235–246. https://doi.org/10.1016/j.actamat.2017.12.023

Zhao, P., Wang, Y., Niezgoda, S.R., 2018. Microstructural and micromechanical evolution during dynamic recrystallization. Int. J. Plast. 100, 52–68. https://doi.org/10.1016/j.ijplas.2017.09.009

Zhou, F., Lee, J., Dallek, S., Lavernia, E.J., 2011. High grain size stability of nanocrystalline Al prepared by mechanical attrition. J. Mater. Res. 16, 3451–3458. https://doi.org/10.1557/JMR.2001.0474
Zhu, L., Lu, J., 2012. Modelling the plastic deformation of nanostructured metals with bimodal grain size distribution. Int. J. Plast. 30–31, 166–184. https://doi.org/10.1016/j.ijplas.2011.10.003

Table captions:

Table 1. Comparison of elongations of the ECAPed Al–7Mg alloy at high temperatures with others reported in literature.

Alloy	Processing	Temperature (K)	Strain rate (s^{-1})	Elongation (%)
Al–7Mg	ECAP	423	5×10^{-4}	~69
Al–7Mg	ECAP	473	5×10^{-4}	~127
Al–7Mg	ECAP	548	5×10^{-4}	~251
Al–7Mg	ECAP	573	5×10^{-4}	~318
Al–7Mg	ECAP	623	5×10^{-4}	~155
Al–7Mg	ECAP	573	1×10^{-2}	~325
Al–7Mg	ECAP	573	1×10^{-3}	~523
Al–4.94Mg–1.53Mn (Masuda et al., 2018)	rolling	723	1×10^{-3}	~320
Al–6.3Mg–0.7Mn–0.3Cr (Portnoy et al., 2013)	rolling	803	5×10^{-3}	~450
Al–4.4Mg–0.4Cu (Soer et al., 2006)	rolling	713	1×10^{-3}	~357